Università
degli Studi
di Padova

Dipartimento di Ingegneria Industriale DII

Corso di Laurea Magistrale in Ingegneria Meccanica

Waterjet Propulsion: Mechanical and Hydrodynamical Design Issues

Relatore
Ch.mo Prof. Ernesto Benini

Laureando
Francesco Guadagnin
Matricola 1078781

Anno Accademico 2019/2020

To the ones who always believed in me,
supporting my choices.

Contents

List of Figures

List of Tables

Nomenclature

Latin

Symbol	Description	Units
a	Speed of sound	$\mathrm{m\,s^{-1}}$
A	Flow section	$\mathrm{m^2}$
A	Planform area of a streamlined body section	$\mathrm{m^2}$
A_c	Cross sectional area	$\mathrm{m^2}$
A_n	Cowl surface area projected normally to its axis	$\mathrm{m^2}$
B	Diffuser area blockage parameter	-
C_L	Lift coefficient	-
C_P	Pressure coefficient	-
C_{PR}	Diffuser static pressure recovery coefficient	-
D	Diameter	m
D_h	Hydraulic diameter	m
e	Fluid internal energy	$\mathrm{J\,kg^{-1}}$
e_r	Relative error	-
f	Darcy friction factor	-

F_L	Lift force	N
F_z	Force component parallel to freestream velocity exerted on the fairing	N
g	Gravitational constant	$\mathrm{m\,s^{-2}}$
h	Fluid specific enthalpy	$\mathrm{J\,kg^{-1}}$
h	Fluid total head	m
h_0	Fluid specific total enthalpy	$\mathrm{J\,kg^{-1}}$
h_f	Waterjet friction head	m
h_t	Work in meter of fluid height delivered by the impeller on fluid	m
i	Incidence angle	rad
k	Integer index	-
Kn	Knudsen number	-
l	Chord length	m
l_{eq}	Equivalent forebody length	m
l_{max}	Distance along the fairing axis between highlight section and fairing maximum section	m
L	Representative length	m
L_h	Hydrodynamic entry length	m
m	Howell factor	-

M	Mach number	-
$\dot{m}$	Waterjet mass flow rate	$\mathrm{kg\,s^{-1}}$
n	Impeller revolutions per minute	$\mathrm{min^{-1}}$
N	Diffuser length	m
N_b	Impeller blade number	-
$NPSH$	Impeller net positive suction head	m
N_s	Impeller specific speed	-
p	Absolute fluid pressure	Pa
p	Wetted perimeter	m
p^0	Fluid total pressure	Pa
p_{atm}	Atmospheric pressure	Pa
p_v	Fluid vapor pressure at fixed temperature	Pa
q	Fluid dynamic pressure	Pa
Q_v	Volumetric flow rate	$\mathrm{m^3\,s^{-1}}$
r	Radius	m
R	Diffuser radius	m
R_{ext}	Magnitude of external forces resultant	N
Re	Reynolds number	-
s	Fluid specific entropy	$\mathrm{J\,kg^{-1}\,K^{-1}}$

t	Blade spacing	m
t_{eq}	Equivalent forebody thickness	m
T	Fluid absolute temperature	K
T	Period	m
T	Waterjet thrust	N
U	Fluid peripheral velocity	$\mathrm{m\,s^{-1}}$
u	Fluid specific internal energy	$\mathrm{J\,kg^{-1}}$
u	Fluid local velocity inside boundary layer	$\mathrm{m\,s^{-1}}$
V	Absolute velocity	$\mathrm{m\,s^{-1}}$
$\overrightarrow{V}$	Fluid absolute velocity vector	$\mathrm{m\,s^{-1}}$
V_s	Vessel speed	$\mathrm{m\,s^{-1}}$
W	Fluid relative velocity	$\mathrm{m\,s^{-1}}$
w_c	Work per unit of fluid mass delivered by the impeller on fluid	$\mathrm{J\,kg^{-1}}$
X	Generic parameter	
x_A	Location of maximum camber along the chord from the leading edge	m
y_A	Maximum camber	m
y^+	Dimensionless wall distance	-

Greek

Symbol	**Description**	**Units**
α	Angle of attack	rad
β	Relative fluid angle with respect to tangential direction	rad
γ	Stagger angle	rad
δ	Fluid deviation angle	rad
Δ	Variation	-
ε	Average wall roughness height	m
η	Waterjet propulsive efficiency	-
η_{id}	Impeller hydraulic efficiency	-
θ	Diffuser wall inclination angle	rad
θ_1	Angle between the chord and the tangent to the mean camber line at the leading edge	rad
θ_2	Angle between the chord and the tangent to the mean camber line at the trailing edge	rad
θ_c	Camber angle	rad
λ_m	Waterjet loss coefficient	-
λ_w	Blade load factor	-
μ	Fluid dynamic viscosity	Pa s
μ_t	Eddy dynamic viscosity	Pa s

π	Ratio between circumference and diameter of a circle	-
ρ	Fluid mass density	$\mathrm{kg\,m^{-3}}$
σ_c	Thoma number	-
τ	Shear stress	Pa
ϕ	Flow coefficient	-
ψ	Pressure coefficient	-
ψ_t	Theoretical pressure coefficient	-
ω	Impeller angular velocity	$\mathrm{rad\,s^{-1}}$

Subscripts

Symbol	**Description**
θ	Tangential direction
0	Total state
1	Impeller inflow section
2	Impeller outflow section
$1d$	Diffuser inflow section
$2d$	Diffuser outflow section
∞	Freestream state
∞, int	Freestream state inside the captured streamtube

a	Adjusted
a	Available
B	Blocked
c	Cross-sectional
e	External impeller diameter, i.e. shroud
Eur	Europe
g	Gravity
h	Hydraulic
hl	Highlight
i	Internal impeller diameter, i.e. hub
i	Initial
k	Generic blade section
l	Chord length
m	Fairing maximum diameter
max	maximum
n	Numerical
ne	Nozzle exit flow section
r	Radial direction
r	Required

t	Theoretical
US	United States
w	Wall
z	Axial direction

Superscripts

Symbol	**Description**
0	Total state
$*$	Incipient cavitation
$*$	Optimum design
$**$	Optimum design
$\overline{X}$	Mass flow average of the quantity X

Abbreviations and acronyms

Symbol	**Description**
CFD	Computational Fluid Dynamics
CPU	Central processing unit
EIA	Energy Information Administration
MCL	Mean camber line
$NACA$	National Advisory Committee for Aeronautics
$RANS$	Reynolds-averaged Navier–Stokes

RMS	Root mean square
SES	Surface effect ship
SST	Shear stress transport
US	United States

1 Sommario

Il presente lavoro affronta le problematiche di carattere meccanico ed idrodinamico relative alla progettazione di un prototipo innovativo di idrogetto per velocità elevate.

Poiché non è stato possibile affrontare le tematiche meccaniche senza fare esplicito riferimento a dati sensibili dell'azienda, queste sono state completamente omesse. Inoltre, la pubblicazione ha comportato la modifica di tutti i dati. Quelli riportati sono inaffidabili.

Le questioni di carattere idrodinamico hanno coinvolto l'analisi della procedura di progettazione preliminare della girante e del modello numerico relativo al suo funzionamento nel punto di progetto. Ciò è stato fatto al fine di comprendere le ragioni alla base delle incompatibilità riscontrate inizialmente dal progettista. Attraverso un'analisi scrupolosa delle assunzioni alla base dei modelli, le principali inconsistenze insite in entrambi sono state identificate. Per il modello teorico, queste sono state attribuite alla scelta di un insieme incoerente di assunzioni. Invece, l'analisi dei risultati del modello numerico ha evidenziato le carenze inizialmente riconosciute per il modello teorico. Inoltre, ulteriori inapropriatezze sono state riconosciute e ricondotte ad una scelta inopportuna delle condizioni al contorno.

È stato possibile effettuare la correzione delle ultime per mezzo dello sviluppo di un modello teorico relativo ai processi subiti dal fluido attraverso il diffusore. Dopo una discussione dei risultati osservati, questi ultimi sono stati utilizzati per modificare il modello numerico iniziale. Significativi miglioramenti in termini di rappresentatività del modello nei confronti del fenomeno fisico osservato sono stati raggiunti.

2 Abstract

Present work deals with mechanical and hydrodynamical issues related to the design of an innovative waterjet prototype for high speeds.

Since it was not possible to address mechanical issues without making explicit reference to confidential company data, these have been completely omitted. For the same reason, company name was concealed. In addition, publication resulted in all data modification. Those reported are unreliable.

Hydrodynamical issues surveyed impeller preliminary design procedure and its numerical model related to in-design operation. This was done to understand reasons behind incompatibilities initially found by the designer. Through a scrupulous analysis of the assumptions underlying both models, main inconsistencies were identified. As far as theoretical model is concerned, these have been attributed to the choice of an inconsistent set of assumptions. Instead, results analysis of the numerical model highlighted deficiencies previously recognized in the theoretical model. Further, extra fallacies were recognized. These were traced back to an improper choice of boundary conditions.

Then, numerical model was corrected through the development of a new theoretical model. This involved the study of the processes undergone by the fluid through the diffuser. After a discussion of the observed results, these were used to adjust initial numerical model. Significant improvements in terms of model representativeness were achieved.

3 Waterjet Propulsion: An Overview

3.1 Operating Principle

A *waterjet* is a device aimed to provide kinetic energy to the craft on which it is installed. This process takes place by virtue of fluid momentum increase between waterjet end sections. In fact, due to the second law of dynamics, a change in fluid momentum results in a force parallel and with the same sense of its acceleration. In addition, this law gives force magnitude that the waterjet delivers on fluid. The corresponding force undergone by the device is called propulsive or *thrust*. Action-reaction law can explain its origin. In fact, this postulate asserts that mechanical interactions between two systems placed in contact occur by means of two equal and opposite forces.

The operating principle of a waterjet can be illustrated referring to the conceptual layout of figure 3.1 [1].

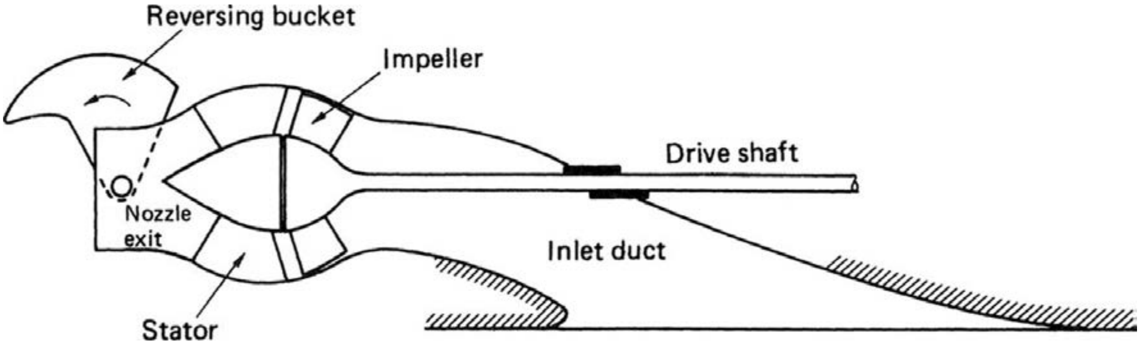

Figure 3.1: *Main waterjet components [1].*

The figure sketches the typical shape of a waterjet meridian duct. In this example the propulsion system is faired into the hull of the vessel.

For a given vessel speed, a fixed amount of the outside fluid enters the waterjet recalled by the impeller depressive action. The *inlet duct* decreases fluid velocity approaching to the inflow impeller optimal value. Because of inlet duct shape, fluid preserves as much as possible its undisturbed characteristics.

Subsequently, the *impeller* increases fluid energy. Amount and distribution of energy transferred depends on impeller type. Yet, much of the total energy exchanged results in fluid static pressure rise. For the impeller to be able to produce this energy transfer, mechanical energy must be transferred to its shaft. This is done by means of a *drive shaft* between this component and the power unit.

Once fluid has been discharged, a second row of *stator* blades may be present. Their purpose is twofold: straighten the flow exiting from the impeller and stiffen hub structure. Straightening purpose is to convert fluid kinetic energy associated with swirl component into a static pressure rise. Indeed, the former does not contribute to thrust generation; yet, the latter does.

Once pressurized, fluid flows spontaneously through the *nozzle*. In fact, process-driving force is the pressure difference between internal and external flows. Thus, through the nozzle a fluid expansion takes place. This continues until external pressure is reached. If fluid mass density is constant, then this expansion produces an increase in jet throughflow velocity. A condition for nozzle design is that at the engine outflow section, fluid velocity be greater than the one at the inflow. In this way, between waterjet end sections a fluid momentum increase is achieved. Thus, for reasons explained, this generates a propulsion.

A *reversing bucket* may be present. This device is actuated mechanically or hydraulically. It spills out part of jet to decrease fluid momentum at the outflow section. In this way, thrust required by the user can be adjusted.

3.2 Component Tasks and Issues

From section 3.1, it is clear that for a waterjet to produce thrust, fluid must increase its momentum. At this purpose, components of figure 3.1 are arranged. All of them has one or more specific functions. Each tasks results from the main one, which is thrust generation. Besides, assumptions about waterjet framework cause other duties to be accomplished. These tasks and the associated issues are examined below. Aspects related with fluid interactions will be put forward.

3.2.1 Inlet

In figure 3.1, the waterjet is faired into the hull. Thus, the only inlet tasks are related to internal hydrodynamics. At the design point, these are basically the following.

1. Incoming water flow regulation, i.e. making a clear distinction between internal and external flow [7], [9], [10]. This ensures that inside the waterjet a defined volume flow rate runs. Its value should be as close as possible to the design one. This fact guarantees that impeller and so waterjet performance are greatest. Underlying relation will be explained later, concerning impellers;

2. Fluid velocity control. Indeed, fluid velocity at impeller inflow must be as close as possible to the impeller design one. Since this is usually lower than the speed of the vessel [11], this means decelerating appropriately the incoming flow.

   If this device is bladeless, then the extension of the inlet must be appropriate. Further, its wall inclination angle must be shallow. In fact, natural diffusion is a rather slow process. These remarks justify inlet proportions and shape as sketched in figure 3.1. In addition, because of the same facts small boats are less suitable for waterjet propulsion [1]. In these cases, it may be useful to provide inlet with blades. In this way, greater deviations are allowed for the same pressure rise achieved. This reduces inlet axial extension, although decreases its efficiency due to higher wall friction;

3. Undisturbed flow characteristics preservation. The inlet has to guarantee that the flow introduced reaches the impeller with minimal distortions. To prevent foreign substances from entering the waterjet, an inlet guard is placed at the entrance [1]. From shielding point of view, it would be advisable for its grid size to be as small as possible. Yet, from hydrodynamic point of view, this fact generates a conflict. In fact, as grid size decreases, pressure losses through the engine increase. This fact reduces overall jet efficiency. At the same time, this can results in cavitation. Furthermore, inlet shape must avoid fluid stall. This phenomenon can generate cavitation, too. As will be explained in section 3.3, this phenomenon narrows waterjet operating range.

For the inlet of figure 3.1, jet inflow section is parallel to freestream velocity. This type of inlet is called *flush* [2].

Ram or *pods* inlet are also used in practice. This sort of inlet is sketched in figure 3.2.

This solution is an attempt to introduce a flow with minimal distortion. As can be seen, this is achieved by arranging inlet section normal to the incoming flow direction. Furthermore, fluid entrance is placed well below the hull. This last fact precludes water near the hull to entry the engine. Indeed, fluid in this region is slowed down due to parietal friction. Therefore, fluid hydrodynamic quality is closer to the undisturbed one. Excluding the

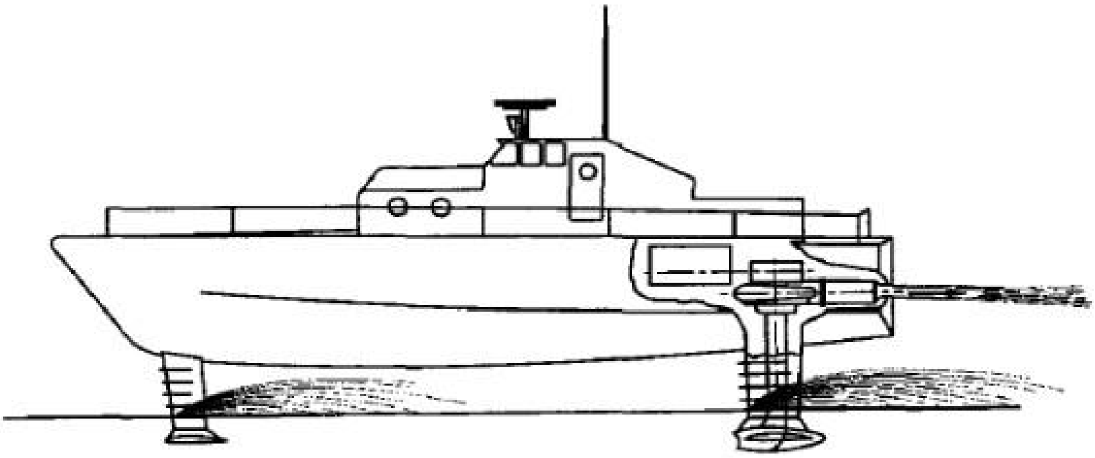

Figure 3.2: *Ram or pods inlet in a hydrofoil [2].*
It is shown the regime operating condition of the hydrofoil. In this application the intake is located well below the hull. As it can be argued, this is aimed to prevent air ingestion. The same problem is found in the surface effect ship (SES).

hydrofoil case, craft hydrodynamic drag is greater due to the increased solid surface exposed to the external flow. This is a major issue in high-speed applications. In fact, inlets of this sort have an additional task: achieve the smallest craft hydrodynamic resistance [9], [10].

A third type of inlet is called *scoop*. It constitutes an hybrid solution between flush and pods. Two models of this sort of inlet are sketched in figure 3.3. Nowadays it is seldom used, despite of their appealing in terms of minimization of flow distortion and total pressure loss. For more details, see [12].

3.2.2 Impeller

Main impeller duty is to transfer rotational kinetic energy supplied by the power unit to the fluid. Efficiency of this process directly affects overall

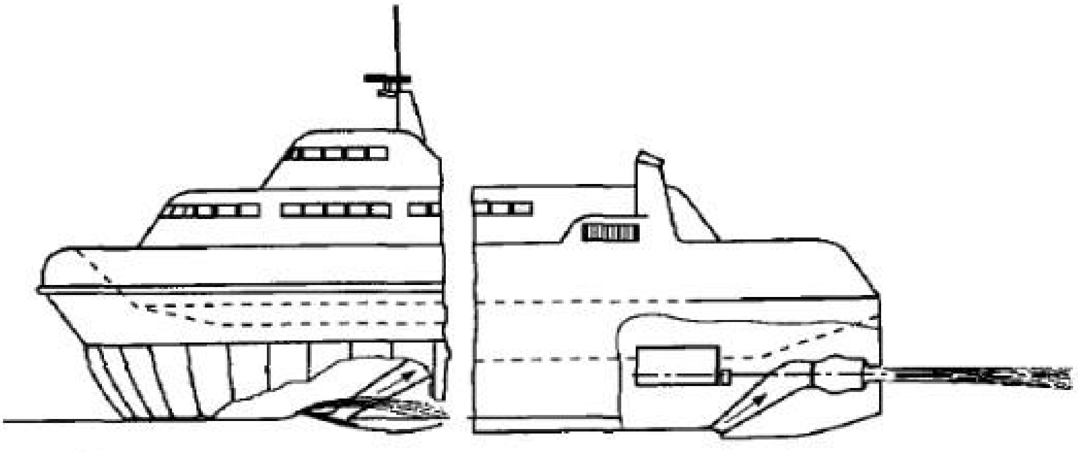

Figure 3.3: *Scoop inlet solutions [2].*
It should be noted that the flow inlet section is at an angle with respect to the freestream velocity. These types of inlets stem from aeronautics experience.

waterjet performance and efficiency. In fact, if hydraulic efficiency reduces, then fluid head decreases. This causes a lowering of fluid total pressure. Then, nozzle expansion results in only a modest increase of fluid momentum. With inflow velocity being equal, this decreases thrust generated by the waterjet. Hence its performance drop. Furthermore, if the energy transmitted to the impeller shaft is unchanged, then overall kinetic energy impressed to the craft falls. *Waterjet propulsive efficiency* is defined as:

$$\eta = \frac{TV_s}{\frac{1}{2}\dot{m}(V_{ne}^2 - V_s^2)} \tag{3.2.1}$$

where T is the waterjet thrust, V_s the vessel speed, $\dot{m}$ waterjet mass flow rate and V_{ne} fluid velocity at the nozzle outflow section [4]. Thus, from assumptions and (3.2.1), it is clear that η decreases.

Experimentation and optimization strategies carried out on an impeller results in an improvement of its performance and efficiency. Yet, this takes long time and efforts. Fluid machinery similitude theory gains these benefits without the expenditure of such a wealth. In fact, it is possible to transfer results related to a reference device to a new one. Hence, this theory simplifies waterjet impeller sizing. Early in the design process, an efficient and performing impeller can be sized, able to meet waterjet needs required. For these reasons, waterjet pumps are typically designed by exploiting similitude results. A model of this type of design will be examined in the next section.

The following results from this theory. A relationship between total energy exchanged, volumetric flow rate, efficiency and angular speed summarizes impeller behavior. Each of these parameters depends on impeller geometry, fluid properties and flow kinematics and dynamics. Dimensional analysis sums up each of these factors by means of one or more dimensionless coefficients. In detail, it is shown that two independent functional relations can represent impeller behavior. These are, for example:

$$\begin{cases} \eta_{id} = f(\phi) \\ \psi = f(\phi) \end{cases}$$

where η_{id} is the impeller *hydraulic efficiency*, ϕ its *flow coefficient* and ψ its *pressure coefficient*. These are defined as functions of impeller operating parameters:

$$\eta_{id} = \frac{h}{h_t} \tag{3.2.2}$$

$$\phi = \frac{\overline{V}_{z1}}{\omega \frac{D_e}{2}} \tag{3.2.3}$$

$$\psi = \frac{gh}{(\omega \frac{D_e}{2})^2} \tag{3.2.4}$$

in which h is the fluid head, h_t the work in meter of fluid height delivered by the impeller on fluid, $\overline{V}_{z1}$ the average absolute velocity at impeller inlet, ω impeller angular velocity, D_e the impeller external diameter and g the gravitational constant.

Furthermore, in-design operating characteristics can be summed up by a single parameter. This is called impeller *specific speed* and it is defined as:

$$N_s = \omega \frac{\sqrt{Q_v}}{gh^{0.75}} \tag{3.2.5}$$

where Q_v is the volumetric flow rate.

Experience proves that several impeller types have acceptable in-design efficiencies only within a narrow range of N_s values. Waterjet type sets impeller volumetric flow rate and head required. Then, once angular speed has been chosen, suitable impeller class for maximizing waterjet efficiency is fixed by N_s value. So, it is clear that for a given impeller exists a unique link between efficiency and flow rate. This justifies discussion made on point 1 of subsection 3.2.1. At the same time, it can be argued that waterjet efficiency depends on that of the impeller. In conjunction with previous remark, it explains the reason why different impeller types are used in commercial waterjets.

Roughly, impeller types for waterjet applications can be divided into three types: centrifugal, mixed and axial flow. These are shown in the figure 3.4.

For specific speed values higher than 7, inducers are used [1]. It should be noted that as the impeller class varies, flow type that takes place within it also varies. This is a consequence of the close correlation between impeller energy exchange and geometry. Thus, names given follow.

3.2.3 Nozzle

Inside the impeller and the nozzle absolute flow undergoes a convective acceleration. However, most of it is generated inside the nozzle. Thus, a fundamental task performed by this component is to increase fluid momentum. To generate the desired thrust, a specific momentum increase is required.

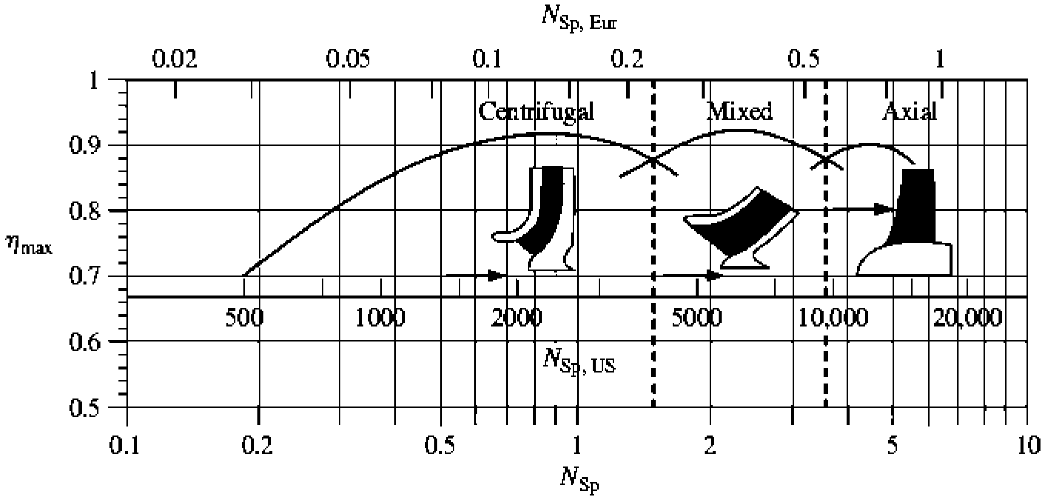

Figure 3.4: *Relationship between impeller specific speed and in-design hydraulic efficiency [3].*

The ordinate expresses the maximum value of impeller hydraulic efficiency based on decades of experience. This value is referred to that impeller having the particular specific speed value read on the abscissa.

Three scales are shown on the abscissa. The lower one refers to the dimensionless specific speed and is referred to as N_{sp}. Instead, the two upper ones refer to the units typically adopted in the United States and in Europe. In United States, it is customary to express parameters of equation (3.2.5) *as: ω [rpm], Q_v [gpm] and h [ft]. Gravitational constant is ignored. In Europe, all quantities are expressed in SI units, with ω in Hz.*

In waterjet in-design condition, flow can be assumed steady. In addition, water can be treated as incompressible. Then, its flow is subsonic. From continuity, it follows that for the fluid to increase its momentum, nozzle section in stream direction must decrease. This explains the convergent geometry that can be seen in the figure 3.1.

The way in which this acceleration takes place affects waterjet performance and efficiency.

This can be justified as follow. The direction of interest for the increase in momentum is that of nozzle axis. If tangent to nozzle profile at the exit were at an angle with respect to nozzle axis, then absolute velocity at the outflow would have a radial component. This velocity component does not contribute to thrust generation. Yet, a form of kinetic energy is associated with it. This energy was obtained at the expense of fluid pressure. As seen, pressure rise is operated by the impeller converting a form of energy communicated as input to its shaft. Thus, a radial velocity component at the outlet represents an energy loss. This loss results in a decrease of waterjet performance and efficiency. Moreover, let us suppose that tangent to nozzle profile at its inlet is different from that at the impeller outlet. Then, in crossing this region, fluid would suffer a loss of pressure due to abrupt deviation. For the same reasons, it is clear that this results in a lowering of propulsive thrust and efficiency.

These drawbacks can be avoided using well-rounded radius at initial and final parts of the nozzle. Tangent to each fillet radius at nozzle end-section must be properly set, as seen. At nozzle inlet, this guarantees a gradual change of direction to the fluid. Instead, at the outlet it ensures that the axial velocity component is prevailing.

3.3 Comparison with Marine Propeller

To gain insight in waterjet potentials, a brief comparison with a very common way of marine propulsion, i.e. marine propeller, is presented.

In section 3.2 it was beheld that waterjet framework consists of a series of components. Each of these is necessary for thrust generation. With power unit being the same, it is rather immediate to grasp that a propeller is a simpler and thus less expensive solution [4].

In fact, at least in the simplest case of a fixed pitch propeller, components number decreases. This results in a lower cost for product design, engineering and manufacturing. Besides, let us suppose that the propulsion system reliability to be guaranteed is the same. Then, single waterjet component reliability must be greater. This results in a more careful choice of materials, manufacturing processes and geometry. Often, these factors raise final product cost.

In addition, it was realized that minimum inlet size is constrained by natural diffusion process features. These facts lead to a greater size required for waterjet installation. Therefore, a higher weight. For these reasons, today their usage is difficult in small boats and in the low-cost market segment [1].

Figure 3.5 shows the propulsive efficiency with vessel speed for different crafts equipped with waterjet installations. This figure summarizes KaMeWa's recent experience [13]. Interpolating these experimental data and analogues relative to propeller efficiencies, figure 3.6 is obtained [4]. Main features of these propulsive systems can be stressed surveying the curves. These trends are well grasped if following facts are considered.

Subcavitating propeller reaches maximum efficiency at low forward speeds. As can be seen from the figure, efficiencies of up to 70% can be achieved at 30 kn. Yet, for higher vessel speeds, efficiency decreases sharply. This is due to cavitation onset.

In fact, for marine applications the velocity ratio between the power unit and the propeller is constant. Then higher vessel speeds result in higher propeller angular velocities. With propeller geometry being the same, this means high peripheral velocities at the blade tip. Under these circumstances, suction pressure on the blade back surface can be as low as local vapor pressure [4].

This gives rise to the formation of micro cavities of vapor within the liq-

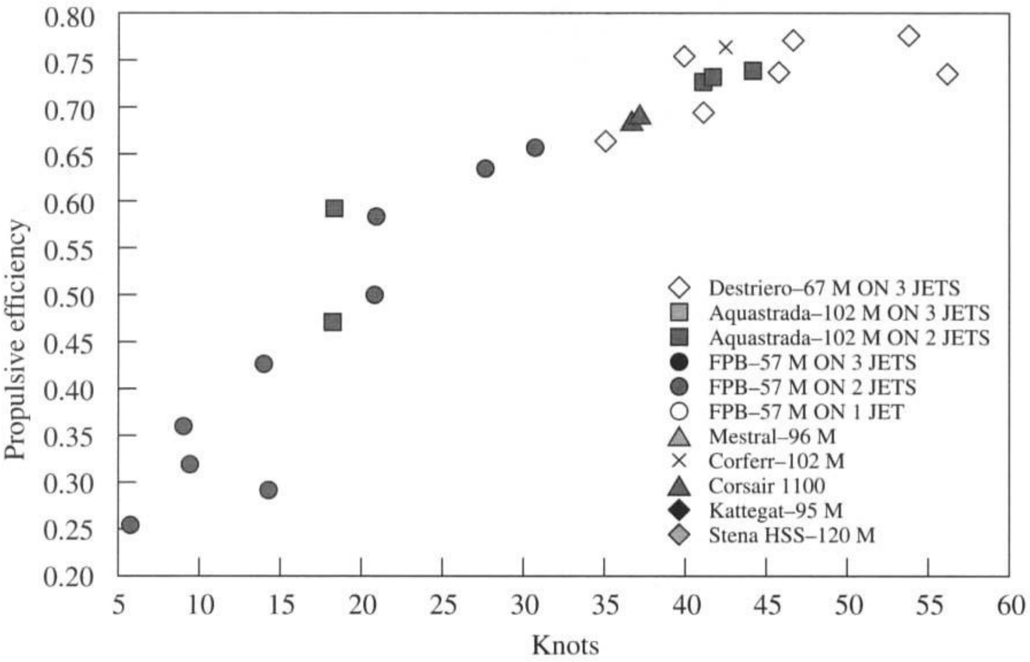

Figure 3.5: *Waterjes propulsive efficiencies as defined in* (3.2.1) *as a function of vessel speed [4].*

All the experimental results plotted are associated to tests conducted on monohulls (symbol M). Details of the experimental procedure followed are available in [13]. In addiction, the author presents other experimental data relating to installations on several vessels. All these support the model assumed in figure 3.6.

uid. These vapor bubbles inhibit thrust generation. As the propeller angular velocity increases, cavitation quickly extends over the entire propeller, starting from blade tip. This phenomenon limits maximum tangential velocity achievable. Indeed, it must be such that the suction side pressure remains above steam pressure value at the operating temperature. Typical values are around 50m/s [4]. Thus, for given propeller dimensions, this places a limit on vessel speed attainable. In commercial vessels, this phenomenon becomes significant for speeds greater than 35kn [4].

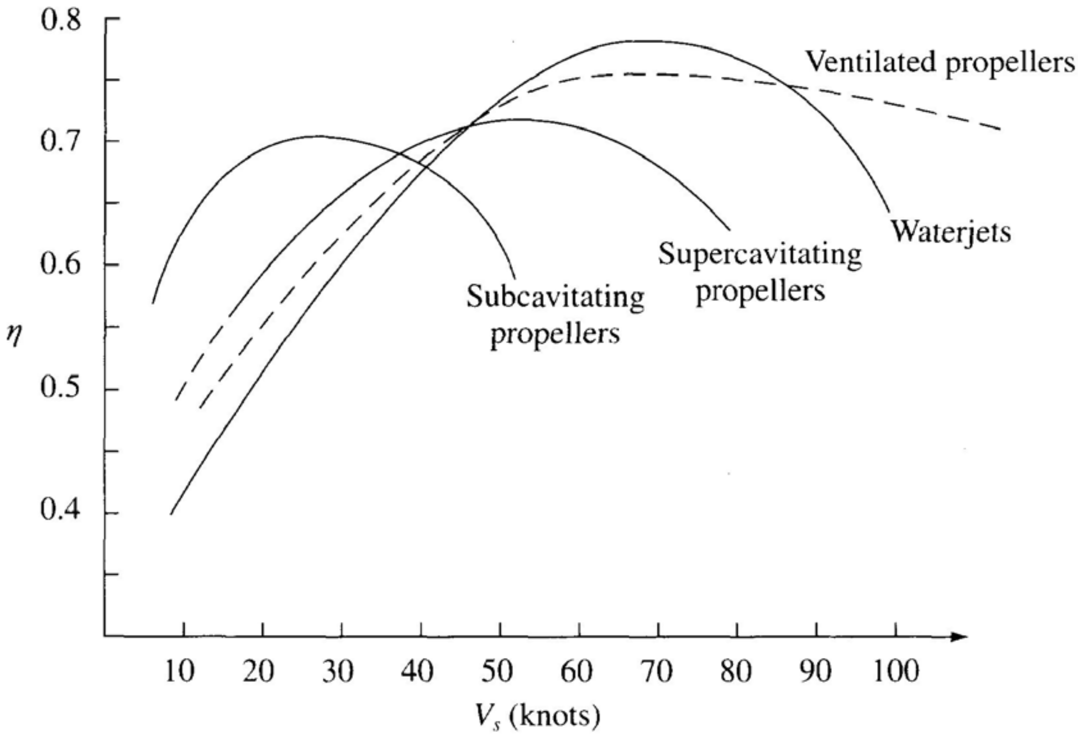

Figure 3.6: *Waterjets and marine propeller systems propulsive efficiencies [4].*

V_s is the vessel speed. η is the propulsive efficiency as defined in (3.2.1). *All curves interpolate experimental data similar to those shown in figure 3.5.*

Propellers can be designed to exploit cavitation. This leads to *supercavitating* or *ventilated propellers* conceptions. In the first case, this allows the operating range to be extended up to high vessel speeds. However, at low speeds operation is inefficient. In fact, a minimum tangential velocity is required to ensure steam cavities formation. Typical lowest values are of the order of 90m/s. At fixed point, this places a limit on smallest vessel speed value. Ventilated propellers are designed to emerge from water during part of their rotation. This permits to reach very high vessel speeds efficiently. At the same time, the operating range is kept wide. Yet, both solutions significantly reduce propeller reliability if compared to subcavitating propeller and waterjet. This is due to structural strength issues. For these reasons these solutions are mainly relegated to competition applications.

Waterjet propulsion has the widest operative range. In fact, water pressurization before its expansion delays cavitation onset. Furthermore, at high vessel speeds there is a range in which its propulsive efficiency is the highest. This can be reached with an appropriate hydrodynamic design [14]. For these reasons, from the 50s on, the interest in commercial applications of waterjets has grown. This regards mainly large ships in relation to fast ferries [15]. In fact, increasing the maximum vessel speed reachable economically allows faster passenger transport. This improves transportation effectiveness. With service cost being the same, this enhances transport attractiveness [14].

3.4 Rationales Underlying the Investigation

In section 3.3, waterjet propulsion benefits on subcavitating propeller were justified. One of these is related to its suitability for use in high-speed transport. In fact, from figure 3.6 it can be argued that waterjet propulsion reaches vessel speed values that are precluded for propeller. Thus, waterjet employment can reduce the time required for people or goods transport.

Increasing data exchange enhances readiness of response to human needs. Implications are many. Further, they embrace a large social scale: from productivity increase of a nation to improvement in life quality of a single person.

In addition, from figure 3.6 it can be noticed that at high vessel speed, waterjet efficiency peaks. Its value is even higher than the greatest of all propeller systems. Reported values could be further increased through research and development. Larger scale diffusion of this propulsive system could eased these activities.

Propulsive efficiency directly affects power train energy consumption. If an internal combustion engine is used, then a decrease in fuel consumption leads to emissions reduction [16]. This holds also for an electric motor. In fact, the majority of the electricity produced today occurs through fossil fuel combustion. This fact can be seen in Figure 3.7.

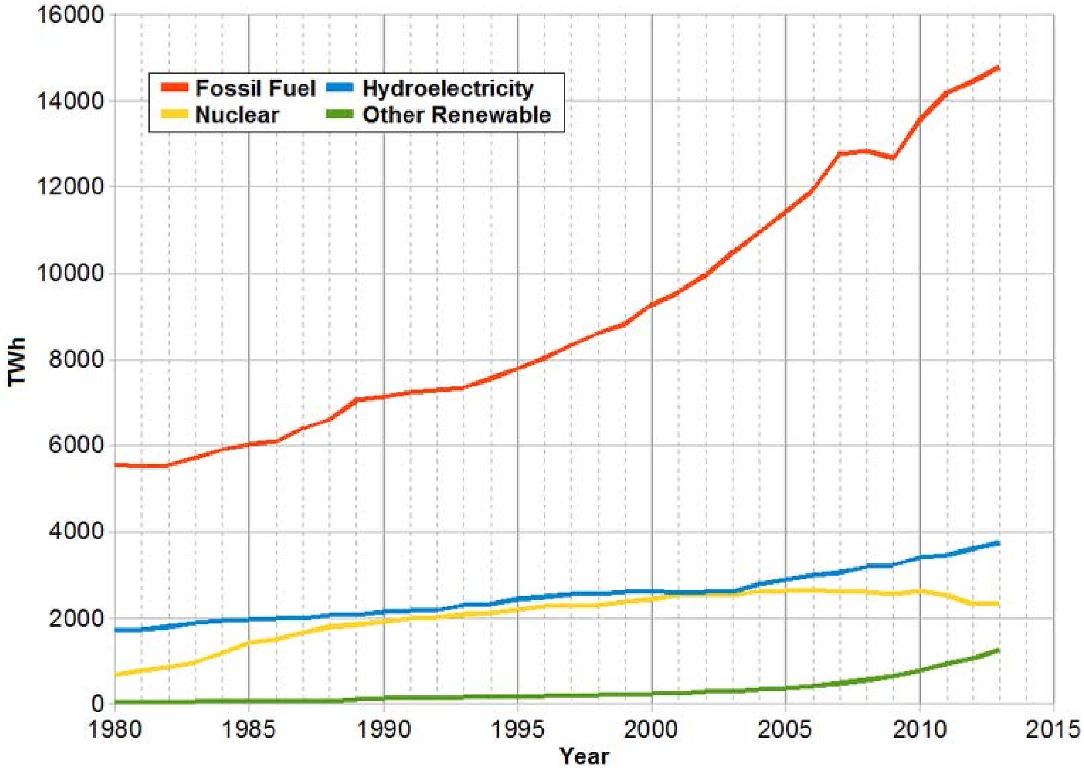

Figure 3.7: *World electricity production by source from 1980 until 2013 [5]. Plotted data were processed starting from those provided by the U.S. Energy Information Administration (EIA). For more details, see [17].*

Nowadays air pollution issues are impelling. In fact, man's harmful emissions have induced irreversible climate changes. These are spread worldwide.

Table 1 shows the distribution of world energy consumption of the year 2012.

Sector	PW h	%
Residential	1.55×10^1	13
Commercial	8.6	7
Industrial	6.51×10^1	54
Transportation	3.05×10^1	26
Total	1.2×10^2	100

Table 1: *World energy utilization by sector in 2012 [8].*
Numerical values reported are sensitive to sector definitions. In this case, EIA definitions were used. For more details, see [17].

It can be seen that transport sector is the second energy user. Central role of this sector can be remarked also by noting that within industry heading, part of the energy consumed is used for transport. Thus, efficient propulsion systems represent an effective way to reduce global energy consumption. In turn, this results in a lowering of emissions.

Waterjet propulsion system asks for a greater space for its installation. Therefore, these systems are heavier than propellers. However, these defects can be contained somehow by using arrangements that are more compact. In particular, waterjet development can be restricted around a single axis: the impeller one. This can be done using a ram type inlet. This would favor small boats installations. Then, extra benefits would result from.

Moreover, a compact solution of this type would bring further advantages with regard to travel comfort. In fact, in this way the entire flow would be moved outside the hull. Thus, acoustic emissions and vibrations generated would decrease. An electric motor adoption would further contribute to reducing them.

The discussion made lead to the following. Waterjet propulsion system constitutes a practical answer to prominent concerns of today's humanity.

Still, in order for these potentials to be realized, it is necessary that waterjet design is carried out correctly. As far as a single component is concerned, this results in such geometry assignment that all its tasks are accomplished efficiently. Furthermore, it is necessary to consider that each task stems from the fundamental one, i.e. thrust production. Hence, mutual influences between components must be accounted for. If neglected, this set of relationships gives rise to unreliable results. Consequently, prediction of a single component in-design behavior is injured.

Present work deals with hydrodynamic and mechanical issues related to waterjet component design. Waterjet type being discussed is for high-speed applications.

The first part of the hydrodynamic problems addressed concerns diagnosis. Reasons underlying lack of compatibility between impeller theoretical and numerical model were recognized. This was managed via a thorough and detailed analysis of the entire design procedure followed. All assumptions made were critically discussed before being accepted. Thus, all detected inconsistencies were explained. Those related to the theoretical model were traced back to the choice of an incoherent set of assumptions. Instead, numerical model errors were attributed to an improper selection of boundary conditions. Then, a theoretical model was conceived. This is aimed to solve numerical model issues. In particular, this model accepts as input in-design impeller data and predicts external and internal diffuser flow features. This method applies fundamental fluid dynamics principles and experimental data related to subsonic diffusers.

4 Preliminary Design of a Waterjet Pump - Theoretical Model Review

4.1 Introduction

Preliminary design of a fluid machine can be defined as the procedure by which its overall dimensions are determined. In order for this method to be applied, some of the operating characteristics that the machine will have must be prescribed. These constitute the so-called project data. They are determined via energy considerations about the plant in which the machine will be inserted.

This procedure is far from possessing the requirements of *exactness* and *uniqueness* typical of exact sciences. In facts, equations used for sizing stem from conservation principles, logical deductions or from optimization criteria. Their number is often lower than unknowns, i.e. parameters values to be assigned.

Parameters values are related to machinery geometry. From the latter depends operating characteristics actually observed. Then, for these to reflect the required expectation, it is necessary a rationale for unknown's choice. To this purpose, experimental experience, research and empirical observations constitute a valuable support. Thus, these contributions provide criteria for the choice of the missing parameters. So, a design procedure able to produce a suitable machine can be completed.

Another feature of the design activity is the *iterativity.* In facts, after the first sample has been manufactured, defects and limitations are recognized. Improvements are therefore conceived. Initially adopted design method or values assigned can be modified. In order for these adjustments to actually constitute improvements, it is however necessary to be aware of their implications on other design variables. Because of the design method intrinsic complexity, in fact, a reasoned change in itself can generate unexpected results. This occurs for example if mutual variable relationships are not taken into account. In addition, a contrast between some of the choices made previously is possible. This can generate logical inconsistencies.

For a theoretical design model is fundamental to be *consistent*. In this way, it can represent a reliable reference to compare later numerical or experimental analyzes. This is crucial to identify any anomalies.

For these reasons, this section examines a theoretical preliminary design model applied to a waterjet axial flow pump.

4.2 An Axial Flow Pump Design Model

4.2.1 Vortex Design Approach of Turbomachinery Blades

In simplified hypotheses defined and discussed below, it is possible to develop a simple theoretical model, able to correlate radial distribution of axial absolute velocity with radial distribution of swirl absolute velocity [7]. This relationship is of central importance in design procedure proposed by Ventrone [18]. Thus, it is appropriate to recall its logical foundations.

Main simplifying hypotheses underlying the discussion follow.

1. Flow is supposed to be steady. So, time dependence of any properties of the fluid is neglected. Hence, turbulence details were forsaken, together with its effects on mean flow. This fact can be considered rightful concerning those regime operating conditions of the pump such that it is allowed to neglect unsteady effects of turbulence. Furthermore, this assumption precludes the possibility of reviewing interactions between the stage under examination and the adjacent one. Indeed, as a conse-

quence of this conjecture, this stage is placed at enough distance from the one examined;

2. Symmetrical flow about the rotation axis of the pump. This hypothesis could be considered rigorously verified for a pump with an infinite number of blades, so that the transversal dimension of the single blade-to-blade duct is infinitesimal. For a real impeller, viz. with a finite number of blades, imposition of this hypothesis implies negligence of the blade-to-blade flow;

3. Incompressible flow. This means that variations in mass density of the fluid due to its pressure variation are ignored. For liquids, this can be considered plausible as long as processes in which sudden variations of pressure with space or with time are excluded from present analysis;

4. Adiabatic flow. From this follows that heat exchanges between flow and impeller are ignored. This fact can be considered plausible as long as the flow can be considered incompressible;

5. Molecular viscosity and thermal conductivity of the fluid are ignored. These hypotheses constitute relevant simplifications in the study of the flow. In fact, imposition of the same hypotheses means to neglect mechanisms of transport of momentum and heat typical of a fluid. These processes take place within viscous and thermal boundary layers, which are for these reasons ignored;

6. Radial clearance between tip and shroud is assumed to be zero. This is a simplification, since recirculation flow that is traditionally observed between tip and shroud or outer casing is ignored. Yet, this hypothesis can be considered verified if it is assumed to transmit the mechani-

cal work necessary to compression through the shroud. In this way, blade tip and shroud can be merged. Traditionally, mechanical work is transferred through the hub. So, a clearance is mandatory;

7. Radial component of absolute fluid velocity is assumed to be zero outside the blade-to-blade duct. Strict respect of this assumption would require a blade of infinite radial extension. However, in the field of axial flow turbomachinery this is commonly considered acceptable. As a consequence of this simplification, stream surfaces are supposed cylindrical upstream and downstream of the impeller;
8. Tangential component of absolute fluid velocity at the impeller inlet is assumed to be zero. This position is accepted if external devices capable of imparting a swirl velocity profile to fluid such as the inlet guide vanes are excluded;
9. Gravity is neglected. This hypothesis is generally accepted in the context of fluid dynamics investigations related to analysis of machine-fluid interactions. In this case, it can be justified noting that pressure increment due to gravity is $\Delta p_g = \rho g D_e = 10^3 * 9.8 * 1.5 \times 10^{-1} = 14.7\text{Pa} = 0.0147\text{mbar}$ Pressure increment operated by the impeller is of *bar* order. Then, for the present case gravity influence is negligible.

If these assumptions can be considered verified, then Navier-Stokes equation in radial direction takes the following form:

$$\frac{\partial p}{\partial r} = \frac{dp}{dr} = \rho \frac{V_\theta^2}{r} \tag{4.2.1}$$

where p is absolute pressure, ρ fluid density, V_θ absolute swirl velocity and r the radius. Furthermore, Euler Turbomachine equation can be written as:

$$w_c = h_{02} - h_{01} = \omega(r_2 V_{\theta 2}) \tag{4.2.2}$$

in which w_c is the amount of specific work that the impeller deliver to the fluid, h_0 is the total enthalpy of the fluid and ω rotation velocity of the impeller. On the other hand, Gibbs equation becomes

$$Tds = du \tag{4.2.3}$$

where T is absolute temperature of the fluid, s its entropy and u its internal energy.

For an inertial observer, total fluid enthalpy is

$$h_0 = h + \frac{|\overrightarrow{V}|^2}{2} = h + \frac{V_z^2}{2} + \frac{V_\theta^2}{2} \tag{4.2.4}$$

Deriving the last with the radius and replacing previous equations within it, it can be deduced that

$$\frac{1}{2}\frac{d(V_z^2)}{dr} = (\omega - \frac{V_\theta}{r})\frac{d(rV_\theta)}{dr} - T\frac{ds}{dr} \tag{4.2.5}$$

Of course, if the fifth hypothesis is verified, then $Tds/dr = 0$.

It is customary to specify a desired swirl distribution downstream of a blade row and calculate the corresponding axial velocity distribution that is supported by the swirl profile. This method of approach is commonly known as vortex design of turbomachinery blades.

If this equation is referred to the impeller outlet section, then a fundamental solution of the previous one can be obtained by imposing an uniform radial distribution of axial absolute velocity. In this case radial distribution of swirl absolute velocity becomes

$$rV_{\theta 2} = cost = \frac{gh_t}{\omega} \tag{4.2.6}$$

This velocity profile is known as a free vortex profile due to its similarity with inviscid and incompressible solution of vortex flow.

4.2.2 A Vortex Design Method

Ventrone [18] offers a simple theoretical model aimed to design an axial flow pump. All assumptions made in previous section are supposed valid. Underlying logical procedure can be divided into three basic parts. Each is defined by a single flow chart.

Main assumptions within each part are justified and commented.

Key: Inputs to the design procedure are enclosed by an elliptical block; assumptions by a square. Adjustment are contained within sharp edges rectangular blocks. Each calculation step is enclosed by a rectangular block with rounded edges.

Part 1. Main dimensions and overall performance of the impeller. Volume flow rate and total head input data are determined by a previous analysis of the plant where the pump is to be inserted. This study depends on the type of plant under exam.

Angular velocity assumption is a compromise between following aspects. The aforementioned design parameter can be chosen in order to maximize pump performance or efficiency. This can be easily understood if classical statistical diagrams are observed. These offer a unique correlation between specific speed and efficiency. A theoretical model can alternatively be developed. This can calculate optimal angular velocity by imposing an optimization condition. Yet, following constraints must be taken into account.

A. If impeller material is fixed, then its mechanical strength is established. This limits peripheral speed maximum value attainable during its operation. Thus, a first constraint is encountered;

B. If the pump is driven directly by an electric motor, then its angular veloc-

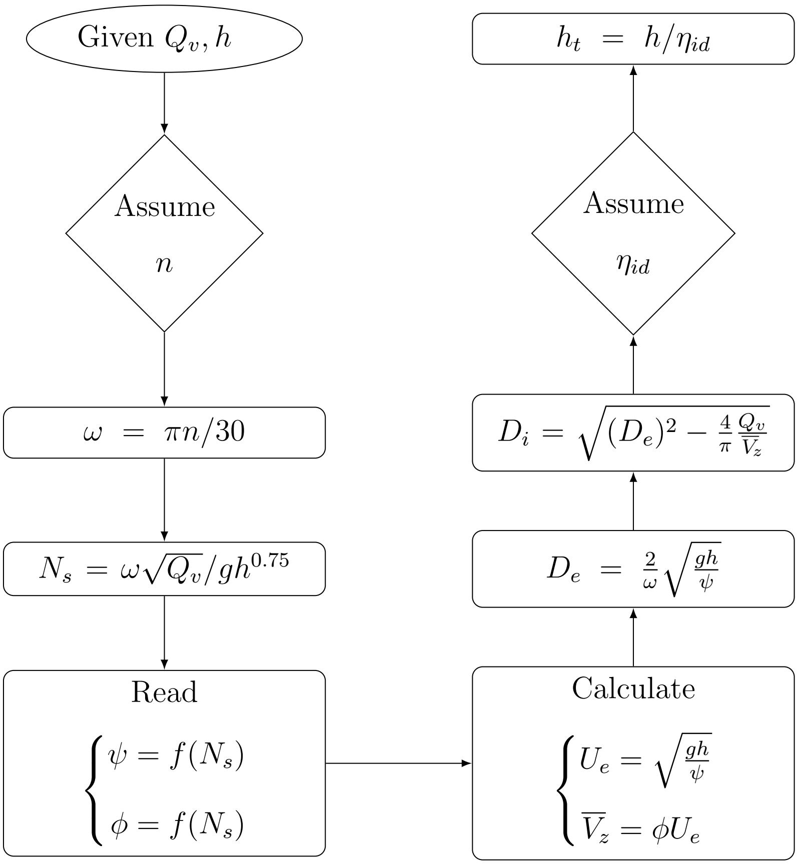

Figure 4.1: *Theoretical design model of an axial flow impeller - Part 1.* *General nomenclature used is defined at the beginning, see page IX. For the block key see page 25.*

ity is equal to the motor one. Latter depends on the motor construction characteristics: mainly number of poles used and characteristics of the electrical circuit used, namely frequency of the electric current;

C. As the rotation speed decreases, main absolute impeller dimensions increase. This implies a greater use of materials and thus increase initial manufacturing costs;

D. As angular velocity increases, pump cavitation tendency increases. This fact can easily be justified by means of the following relationship: $\sigma_c = 0.25 N_s^{1.4}$. This is a result of statistical surveys on a large number of pumps with a global efficiency not less than 0.8.

For these reasons, a feasibility study is required to select design rotational regime. In this analysis, phenomena considered are controlled by observing numerical values assumed by the parameters introduced in the flow chart. Typically, its result is a trade-off between various aforementioned phenomena.

Values for ψ and ϕ can be read in statistical diagrams, such as [18].

If assumed efficiency value can lead to consistent results, then it is necessary to consider the relationship between hydraulic efficiency and specific speed. Again, this correlation is a statistical result, based on a large number of machines [19]. Results obtained in this part, i.e. external and internal impeller diameters, are assumed to be constant along the rotation axis. This is true for the entire impeller axial development.

Part 2. Mean camber line blade geometry definition at the tip. Assuming a free vortex distribution for the outlet swirl absolute velocity is a simple solution to the equation (4.2.5) of section 4.2.1. Indeed, it implies that specific work delivered by the impeller on fluid is constant along the radius. From this and from hypothesis 8 of section 4.2.1 it can be inferred that downstream radial distribution of axial absolute velocity is constant. Furthermore, by imposing continuity equation, it can be deduced that downstream axial absolute velocity is equal to the upstream one. Because of the reduction of design costs and efforts, many pump manufacturers initially adopted this solution. Yet, nowadays more complex solutions are preferred, depending on design goals.

The largest value that can be assumed for the lift coefficient at the tip

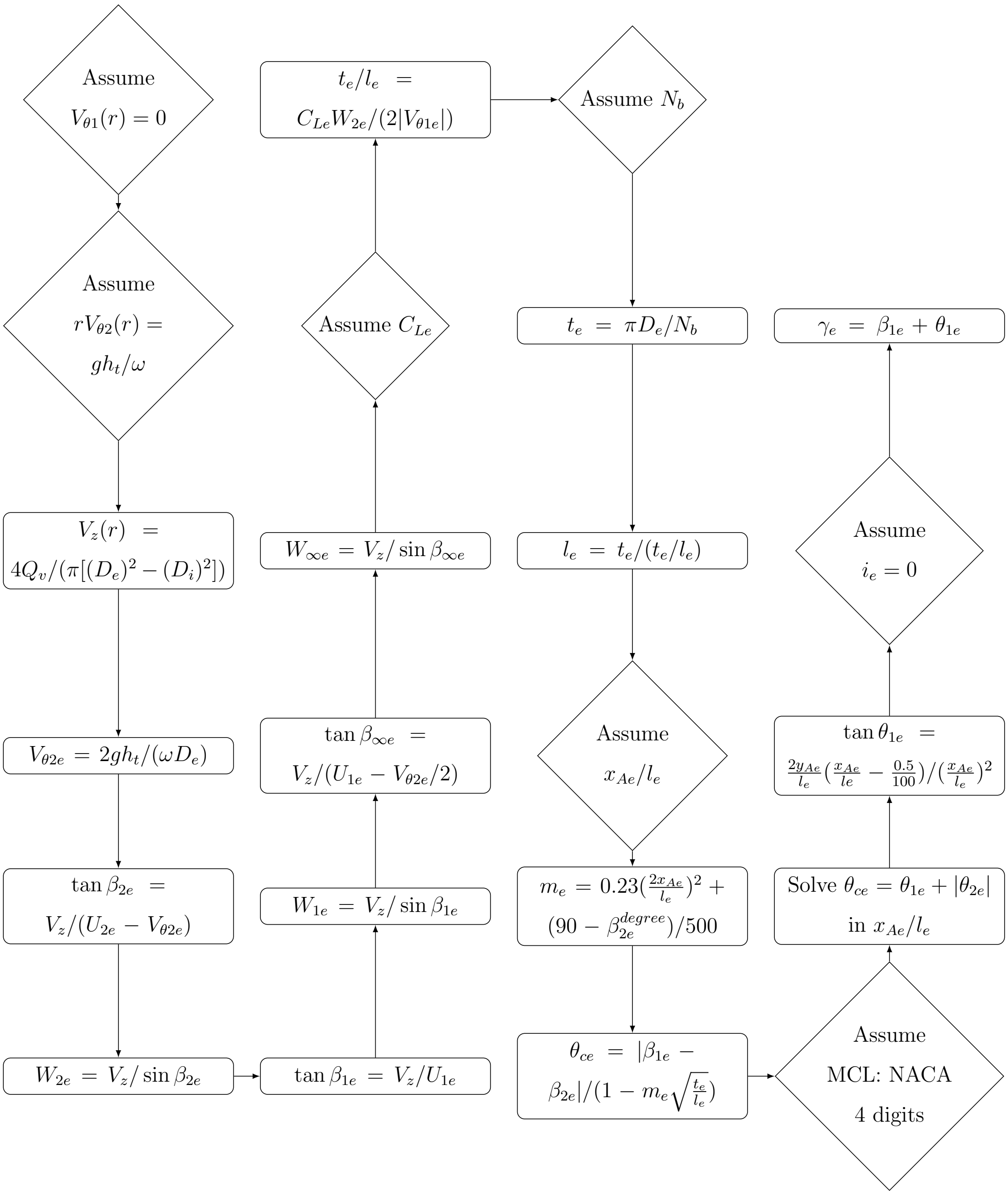

Figure 4.2: *Theoretical design model of an axial flow impeller - Part 2.* *General nomenclature used is defined at the beginning, see page IX. For the block key see page 25.*

is limited the risk of cavitation. To avoid this problem, a reference value of 0.3 can be adopted. Also, the assumed value of the lift coefficient at the hub is critical. In fact, here peripheral speed is minimal. If a free vortex swirl distribution is adopted at the outlet, then tangential absolute velocity is also greatest. Since axial absolute velocity remains constant with radius, this implies that hub relative velocity is smallest. Thus, relative current deceleration through the impeller is greatest therein. This implies a greater risk of stall.

Number of blade assumption is also a result of a compromise between following facts. In fact, as it decreases, circumferential pitch increases. Since solidity is fixed, this implies a contextual increase of the chord. Therefore, pump axial extension increases. Conversely, if the number of blades increases, then hydraulic efficiency decreases, since wall friction losses on the surface of the blades increase.

Assumptions on the camber position, camber value and incidence must be coherent. In fact, high values of camber and of incidence cause mean line curvature to increase. As mean line curvature and incidence increase, energy exchange performed by the profile increases, but stall probability increases. The occurrence of this phenomenon causes a sudden decrease in pump performance and efficiency. Therefore, it can be concluded that high value of camber, i.e. of the mean line curvature, can admit only a modest incidence. Conversely, low curved profiles can adopt even high values of incidence.

Part 3. Mean camber line blade geometry definition at remaining sections. Once middle line geometry was defined for a fixed number of sections, it is necessary to choose a turning center. Often this choice is dictated by the need to obtain a blade geometry free from surface irregularities. Design procedure determine then profile thicknesses to be assigned and their distribution. This problem is mainly of a structural nature and will thus be omitted.

4.3 Review of a pseudo-Ventrone Design Model

An axial pump design procedure for a waterjet engine was reviewed. Logical steps followed by the designer are summarized in the following flow charts. To ease comparison with the procedure defined above, same subdivision was maintained. Yet, the last two parts were merged. This choice was made to highlight differences between this method and the one proposed by Ventrone. Although the method adopted is inspired by Ventrone's procedure, some differences can be noted. This is especially true for the assumptions of design parameters. In addition, the same chart presents one ad hoc adjustment. Furthermore, designer imposed *a posteriori* adjustment, subsequently the creation of blade geometric model. All differences are discussed below.

Part 1. Main dimensions and overall performance of the impeller. As input, main impeller dimensions and the average value of absolute flow velocity were chosen. This choice is motivated by the nature of the plant the pump is to be inserted. Indeed, overall compactness is particularly important for the waterjet in question. Thus, overall pump dimensions have to comply with this requirement. Yet, reaching a well-defined forward speed for the boat on which the engine is installed is of utmost significance. Since this speed is related to the flow velocity through the jet, this requirement can be understood.

Because of these choices, flow and pressure coefficient are deduced rather

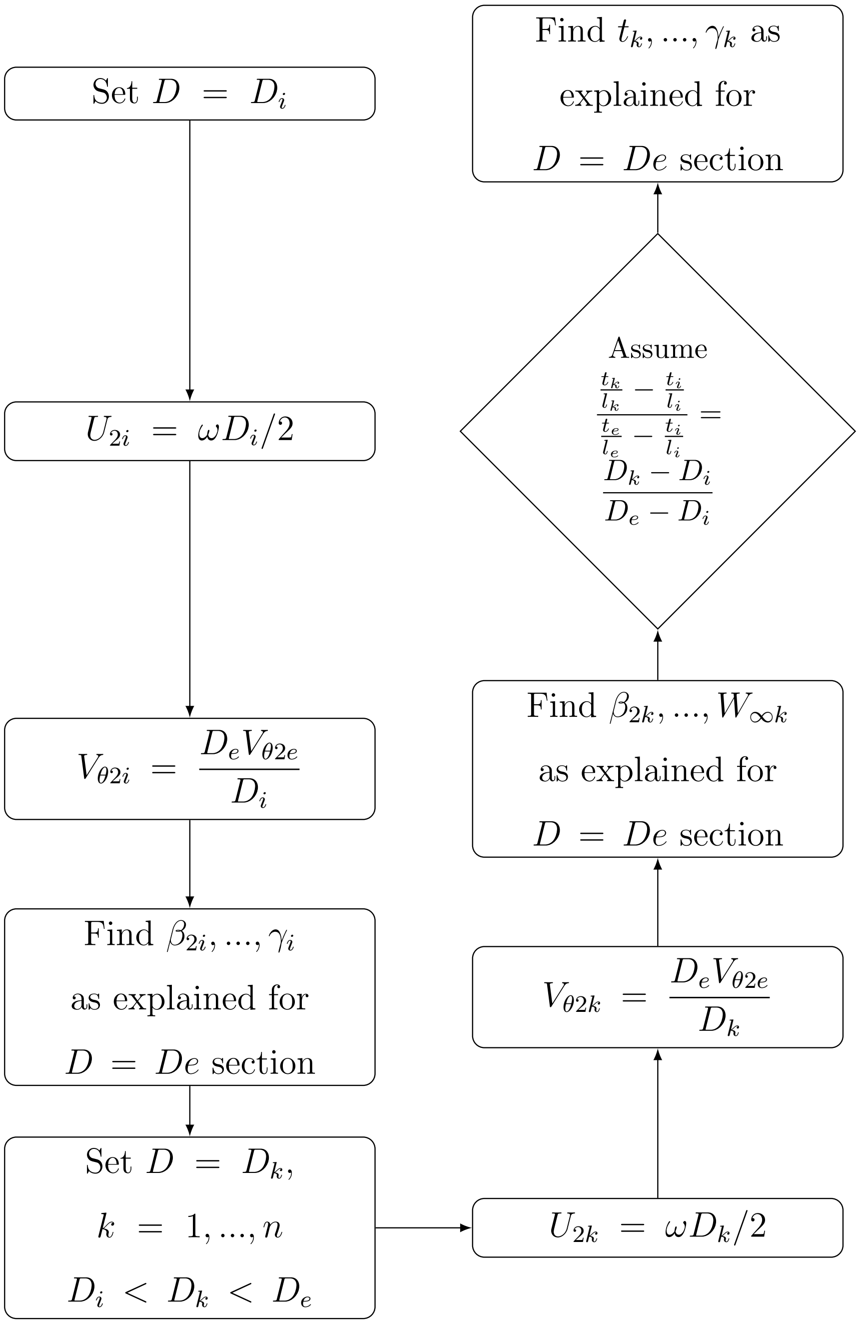

Figure 4.3: *Theoretical design model of an axial flow impeller - Part 3.* *General nomenclature used is defined at the beginning, see page IX. For the block key see page 25.*

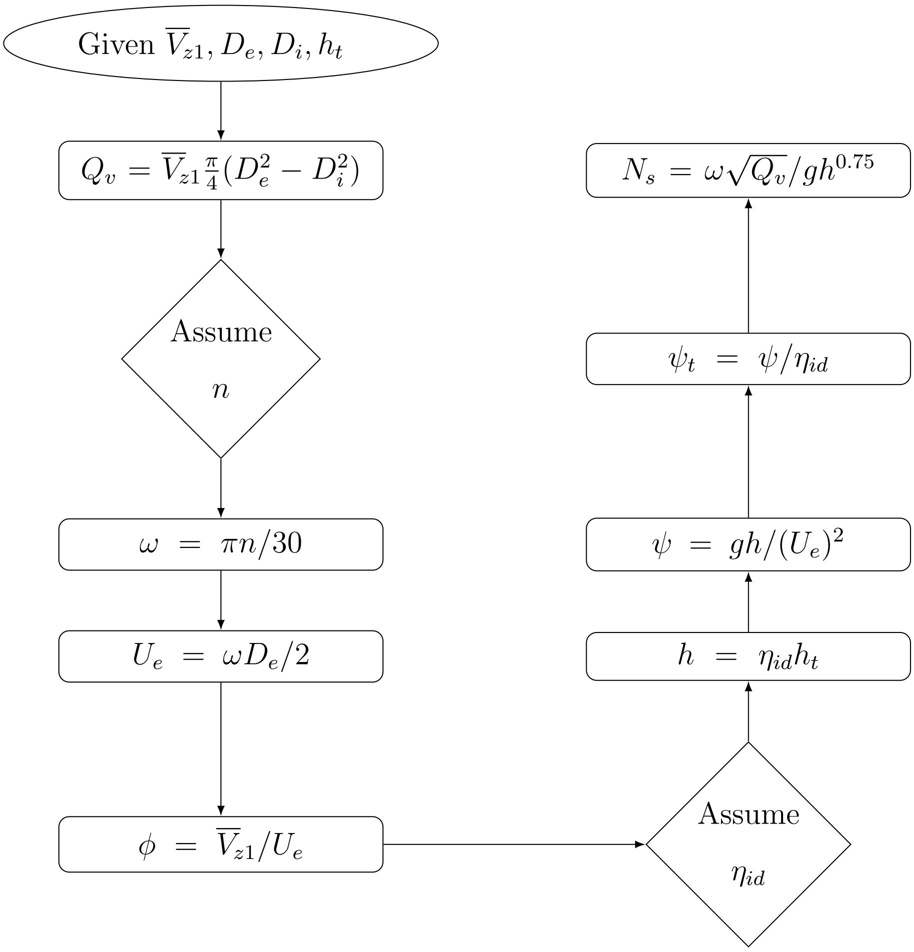

Figure 4.4: *Logical steps followed in preliminary design stage - Part 1.*
General nomenclature used is defined at the beginning, see page IX. For the block key see page 25.

than chosen. This fact is a significant distinction with respect to Ventrone's procedure. In fact, in the latter case the possibility of achieving the performances imposed in the project is ensured by experience. Instead, in the case considered the only parameter that can stem from experience is pump hydraulic efficiency. Hydraulic efficiency value assumed was compared with the one read in[19]. It was argued that neither for this parameter experience support was considered. The criterion used for assuming hydraulic efficiency value was concealed by the designer.

All values assumed in this part are summarized in table 2.

Symbol	Value	Unit
$\overline{V}_{z1}$	8	m/s
D_e	1.5×10^{-1}	m
D_i	0.2×10^{-1}	m
h_t	7	m
n	1.5×10^{3}	rpm
η_{id}	0.4	1
N_b	8	1

Table 2: *Assumed values in preliminary design stage - Part 1.*

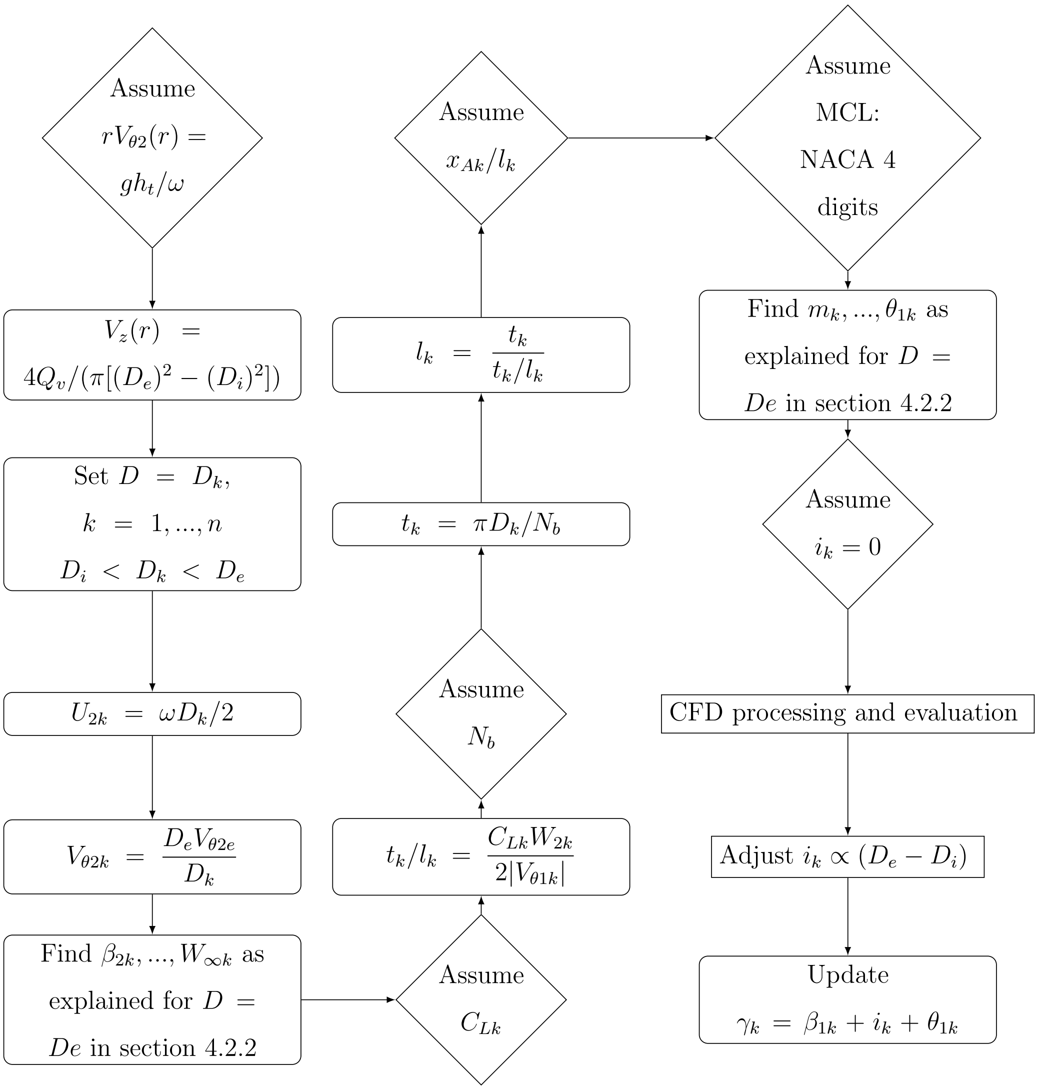

Figure 4.5: *Logical steps followed in preliminary design stage - Part 2.* *General nomenclature used is defined at the beginning, see page IX. For the block key see page 25.*

Part 2. Mean camber line foils geometry definition. Unlike Ventrone, the same definition procedure was applied for each blade section. In particular, it is observed that lift coefficient values were assigned for each foil. These values respect considerations made in previous section. Thus, cascade's radial solidity profile was inferred rather than assigned. This choice exploits to a greater extent geometry freedom in order to obtain a closer control of individual profiles performance. Consequently, performance of the blade as a whole can also be better adapted to the context in which the machine is inserted.

Finally, a radial distribution of incidences was imposed. The profile chosen is proportional to the blade radial extension. This change was imposed as a consequence of a first in-design check with a numerical code. It was aimed to increase energy exchange operated by the blade. Following this refinement, stagger angle value was adjusted.

Values assumed in this part are presented in table 3.

Normalized span	C_{Lk}	$\frac{x_{Ak}}{l_k}$	i_k [°]
0	0.62	0.2	0
0.25	0.62	0.2	4
0.5	0.62	0.2	8
0.75	0.62	0.2	12
1	0.62	0.2	16

Table 3: *Assumed values in preliminary design stage - Part 2.*

4.4 Results Discussion

Main results regarding blade section geometries are summarized in table 4.

Among γ_k, θ_{2k}, β_{2k} and δ_k following relation holds, cfr. figure 4.6:

$$\gamma_k + |\theta_{2k}| = \beta_{2k} + \delta_k \tag{4.4.1}$$

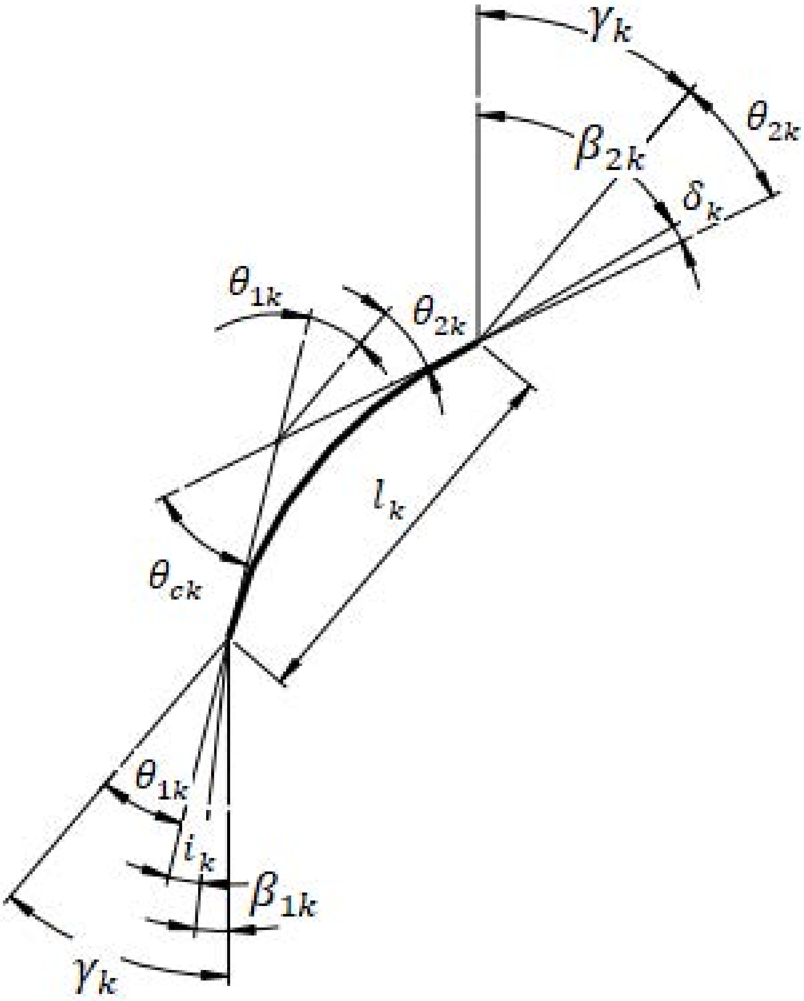

Figure 4.6: *Relationship between blade and flow angles.*
Cylindrical section view of the generic mean camber line (MCL). Thicker line is MCL. Rotational sense is supposed downwards. Hence, pressure side is in the convex side. This justifies δ_k dimensioning. All angles are referred to the tangential direction.

Yet, from table 4, it can be noted that this relationship is not respected. In the theoretical model developed, this is an inconsistency.

An explanation for this self-contradiction can be given with present ar-

Normalized span	t_k [dm]	l_k [dm]	y_{Ak}/l_k [10^{-2}]	x_{Ak}/l_k	θ_{1k} [°]	γ_k [°]	$\lvert\theta_{2k}\rvert$ [°]	β_{2k} [°]	δ_k [°]	$\gamma_k + \lvert\theta_{2k}\rvert - (\beta_{2k} + \delta_k)$ [°]
0	0.20	0.70	9.00	0.2	17.76	27.57	0.23	72.45	5.35	0
0.5	0.70	0.70	2.00	0.2	13.57	83.23	0.72	51.02	3.18	3.75
0.7	0.94	1.00	1.00	0.2	17.82	75.73	0.4	38.84	1.79	7.8
0.75	1.80	1.20	0.5	0.2	15	92.11	0.33	31.16	1.03	11.75
1	1.90	1.50	0.3	0.2	0.63	50.76	0.8	25.93	0.63	17

Table 4: *Theoretical model results - Design parameters.*

gument. It can be argued that residuals are equal to the incidence profile imposed *a posteriori*. Let us suppose that blade section geometries are kept. Then, for the equation (4.4.1) to be satisfied, fluid angles at the impeller exit and fluid deviation must change. In fact, fluid angles at the impeller exit depend on the assumed incidence profile. This can be shown as follows.

From (4.4.1):

$$\delta_k = \gamma_k + |\theta_{2k}| - \beta_{2k} \tag{4.4.2}$$

But:

$$\gamma_k = \theta_{1k} + \beta_{1k} + i_k \tag{4.4.3}$$

Using Howell correlation [20] for δ_k:

$$\delta_k = m_k \theta_{ck} \sqrt{\frac{t_k}{l_k}} \tag{4.4.4}$$

where m_k depends solely on blade geometry:

$$m_k = 0.23(\frac{2x_{Ak}}{l_k})^2 + \frac{90 - \beta_{2k}^{degree}}{500} \tag{4.4.5}$$

Inserting (4.4.5) in (4.4.4) and together with the (4.4.3) in the (4.4.2) it can be deduced that

$$\beta_{2k} = \frac{\theta_{1k} + \beta_{1k} + i_k + |\theta_{2k}| - [0.23(\frac{2x_{Ak}}{l_k})^2 + \frac{90}{500}]\theta_{ck}\sqrt{\frac{t_k}{l_k}}}{1 - \frac{\theta_{ck}}{500}\sqrt{\frac{t_k}{l_k}}} \tag{4.4.6}$$

This relation shows that β_{2k} depends on geometric parameters, incidence and inlet flow angle. If external devices such as inlet guide vanes are excluded, then $V_{\theta 1k} = 0$. Moreover, if absolute average axial velocity value chosen is maintained, then β_{1k} are fixed. Hence, β_{2k} depends only on i_k.

From

$$\delta_k = \theta_{ck} - \theta_k = \theta_{ck} - |\beta_{1k} - \beta_{2k}| \tag{4.4.7}$$

it can be deduced that the variation undergone by β_{2k} affects also δ_k. This can also be argued from equation (4.4.2).

Thus, it has been shown that incidence profile imposed generates an inconsistency in fluid angle values at the outlet. Moreover, β_{2k} values are determined as a consequence of the swirl distribution chosen. Then, it is concluded that the imposition $i_k \propto (D_e - D_i)$ is incompatible with the downstream desired swirl distribution. If blade geometry is kept, then absolute swirl distribution generated with this change cannot be considered vortex free. If blade geometry is to be conceived according to vortex design criteria, then the entire design method related to the definition of the mean camber lines must be reviewed. This regards re-examination of logical steps reported in figure 4.5.

5 Numerical Model Survey

5.1 Introduction

Theoretical model proposed in section 4 results in a preliminary design of the impeller. This procedure takes into account main phenomena that occur during pump operation. Yet, relative entity of these phenomena is influenced by simplifying assumptions made. Furthermore, some phenomena that affect impeller performance and efficiency have been ignored. Turbulence is one of those. This was done due to its intrinsic complexity. Consequently, its analytical description is involved. All phenomena examined and the complex ones can be described with a fluid-dynamic numerical model. In particular, this model was developed to examine previous phenomena's influence on impeller energy exchange and efficiency.

A numerical code requires a certain number of conditions to be specified at fluid domain boundaries. In fact, from numerical point of view, it is necessary to close all the equations used relating to fluid flow. The way this closure is accomplished influences strongly numerical solution quality. Indeed, it can also make the solution impossible to obtain, due to numerical convergence problems.

It is imperative for results to be *reliable*. To this aim, constraints assigned as input must be representative of the physical phenomenon surveyed. Thus, these data should be necessary and sufficient to identify operating condition of interest. If conditions chosen are well-posed, then an experimental reproduction should be allowed. Besides, results should be *accurate*. In fact, output solution accuracy depends on those of the informations supplied as input. A set of boundary conditions of this kind reflects the real problem. Thus, input data accuracy is a necessary condition for the results to be accurate.

Results accuracy and reliability are fundamental for several reasons. In fact, their importance is crucial for an accurate assessment of waterjet characteristics. Indeed, due to constraints on computational resources, a complete waterjet simulation can be unfeasible. Therefore, each component is singularly modeled. Moreover, very often resources only allow the simulation of a part of it. Therefore, numerical results obtained for a component can be used to close the numerical problem of the one downstream. In other cases, results can be used as basis for considerations other than fluid dynamics, such as structural or performance optimization.

This section develops a detailed survey of the numerical model developed for the impeller designed in section 4. The aim is to verify its appropriateness. Assessment criteria used are those mentioned above. Particular importance was given to the discussion of the hypotheses adopted.

5.2 Computational Domain Definition

To consider flow three-dimensional features, a three-dimensional geometric model was used. For the numerical model results to be reliable, fluid domain chosen has to respect some basic details. These are analyzed below, together with main geometric choices adopted.

Blade Geometry Definition. The blade was drawn using the results obtained from previous section. In detail, if values of inlet and exit blade angle and mean camber line are known, then it is possible to draw blade profiles at the reference sections. Thickness distribution was assigned following structural considerations explained in Ventrone. However, quantitative result obtained was concealed by the designer.

Then, the position of profile's turning center was established. Blade geometry was then completed by tracing the envelope surface to the profiles. If blade geometry thus obtained presented surface irregularities, the position of the turning center was changed. The envelope was then repeated. The quantitative result obtained was however concealed by the designer.

Other Boundaries. The other boundaries were defined following these considerations.

A. Turbomachine geometry is periodic along the tangential direction. In general, this does not imply that the flow has the same symmetry property. However, at the design point, all flow properties along the tangential direction can be modeled as periodic functions with period

$$T = \frac{2\pi r}{N_b} \tag{5.2.1}$$

where r is the generic radius [21]. This allows lessening the numerical calculation domain. Thus, computational time can be reduced, without affecting results reliability. For this reason, flow was studied within a single blade-to-blade duct. Boundaries between two adjacent blades were defined as middle geometric surfaces. This choice is typical in turbomachinery computational fluid dynamics (CFD) analysis [22];

B. A physical limit to the extension of the fluid volume is the hub. Therefore, this boundary shape must correspond to the hub one. The hub was supposed to be cylindrical;

C. The shroud places a second physical limit. Maximum radial extension of the fluid domain was assumed equal to the maximum blade radius. This means that radial clearance between the end of the blade and the shroud is zero. This fact may constitute a simplification if it is considered that recirculation flow is in this way ignored. But, this assumption can be accepted if the impeller is driven through the shroud, as discussed in 4.2.1;

D. At the inlet, the flow was assumed undisturbed. This is a simplification. Indeed, for the results to be mostly realistic, in principle fluid conditions in fluid-impeller interaction should be as close as possible to real ones. In a waterjet, the fluid crosses the diffuser before arriving to the impeller. On its surfaces establishment and growth of the boundary layer takes place. Then it follows that the flow upstream of the impeller is not free-streamed. To compensate for this discrepancy, the distance between the fluid inlet section and the front of the blade must assume a minimum value. Typically, it is greater than real impeller extension to consider this fact. Details about the distance chosen was omitted by the designer;

E. The outflow section should be placed at enough distance from the trailing edge of the largest blade profile. In principle, the value to be adopted for this quantity should allow relative speed profile to cancel local speed defect that can be observed near the tail of each blade profile. This velocity defect is due to the presence of a turbulent wake. Because velocity homogenization takes place through turbulence, this process requires some time. If the throughflow velocity is fixed, it is therefore required a well-defined length. This length is the one discussed. Furthermore, its size depends on the extent of the turbulent wake. If stall occurs at the same position along a profile, then characteristic dimensions of this region scales with profile thickness. Thus, all other conditions being equal, the thicker the blade, the greater the distance. Quantitative information about this aspect was concealed.

Considerations made lead to the fluid domain represented in the figure 5.1. This falls within typologies typically adopted for numerical modeling of turbomachinery flows.

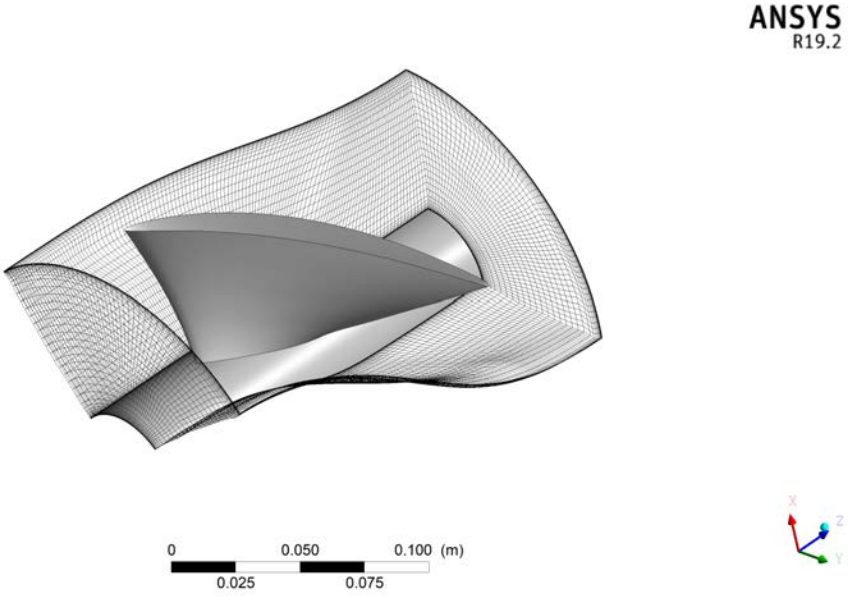

Figure 5.1: *Computational fluid volume.*
Gray surfaces are solid boundaries. Gridded are fluid ones. Shroud is omitted. Flow sense is along Z. Rotational sense is from Y to X.

5.3 Grid Generation and Evaluation

5.3.1 Mesh Topology

From figure 5.1, it can be argued that some boundaries are not contained within coordinated planes. From the grid generation point of view, the *domain geometry* is thus called *complex.*

Cartesian discretization techniques based on the approximation of the geometry would compromise the accuracy of the results obtained. Besides, these methods would represent a waste of computational resources. For some arguments to support these facts, see for example Versteeg [23]. Thus, the usage of a Cartesian grid is precluded.

For the present purpose, it was decided to use discretization methods developed specifically to deal with complex geometries. These methods generate a one-to-one relation between physical domain and a simple computational domain. This is done by means of a suitable coordinate transformation. The computational domain thus generated has a simple form, i.e. all the boundaries are parallel to the new reference system chosen. Once this mapping is complete, mesh generation is performed using a Cartesian method.

In this way, physical domain meshing can take place without any approximation. If the same resources are employed, then this allows higher accuracy in the results compared to the Cartesian mesh generation. Furthermore, mesh and physical domain extension are equal. Coarser grids can then be used, the accuracy being equal. Thus, computational resources are used more efficiently. If a single transformation is used for the entire calculation domain, then the *mesh* is said *structured or body fitted.*

Yet, these methods increase time necessary for numerical model development. This is due to the extreme care necessary for mesh generation. In addition, subsequent discretization of the equations of motion is cumbersome. In fact, the transformation used affects the computational domain generated and so the distribution of the grid lines. Once anti-transformed, it can present regions with distorted cells or with very high aspect ratios. Ultimately, this can cause numerical instability phenomena. Furthermore, grid refinement is purely global. Hence, nodes added to obtain locally higher resolution would necessarily be added in other regions. This represents a waste of computational resources. Prevention of these phenomena forces the user to examine the generated grid and eventually to modify it manually. This step can occupy over fifty percent of the time necessary for the development of the numerical model.

These drawbacks can be reduced somehow using the so-called *block-structured grids*. Physical domain can be partitioned into a discrete number of regions. Partition used is called *mesh topology*. A single geometric transformation can be applied to each of these regions. Constrains are to be defined to assure absence of intersection with the adjacent regions. The result thus produced consists of a discrete set of grids.

Each grid can be conceived and modified individually. Partitions can be made in order to simplify the subsequent discretization of the equations of motion. In this way, central processing unit (CPU) time is reduced. Also, partitions can be adjusted to avoid regions with distorted cells or with an inconvenient aspect ratio. Moreover, this meshing strategy allows local enrichment of nodes. This can be exploit in regions where a greater accuracy of the solution is desired. In this way, computational resources efficiency is improved. The ability to deal with complex geometries is ensured by the use of coordinates transformations.

For these reasons, a block structured mesh was chosen. ANSYS TurboGrid unravels much of partition complications. Also, it eases generation of the geometric transformations. These aspects contain the time necessary for the development of the numerical model. This software has been specially developed to mesh fluid domains typically adopted for numerical flow modeling of turbomachinery. TurboGrid allows the user to automate the choice of the topology of the mesh. This is based on the blade input geometry and it is aimed to guarantee following performance parameters.

Proper description of momentum transport phenomena near solid walls is crucial for performance and efficiency prediction. For this reason, mesh lines should form right angles with solid boundaries. Moreover, skewness and aspect ratios must be controlled to avoid numerical instability.

TurboGrid meets these requirements by generating an automatic mesh topology. This topology is unique for all blade sections. Yet, TurboGrid can vary the extent of individual regions to tailor mesh topology to blade section geometry.

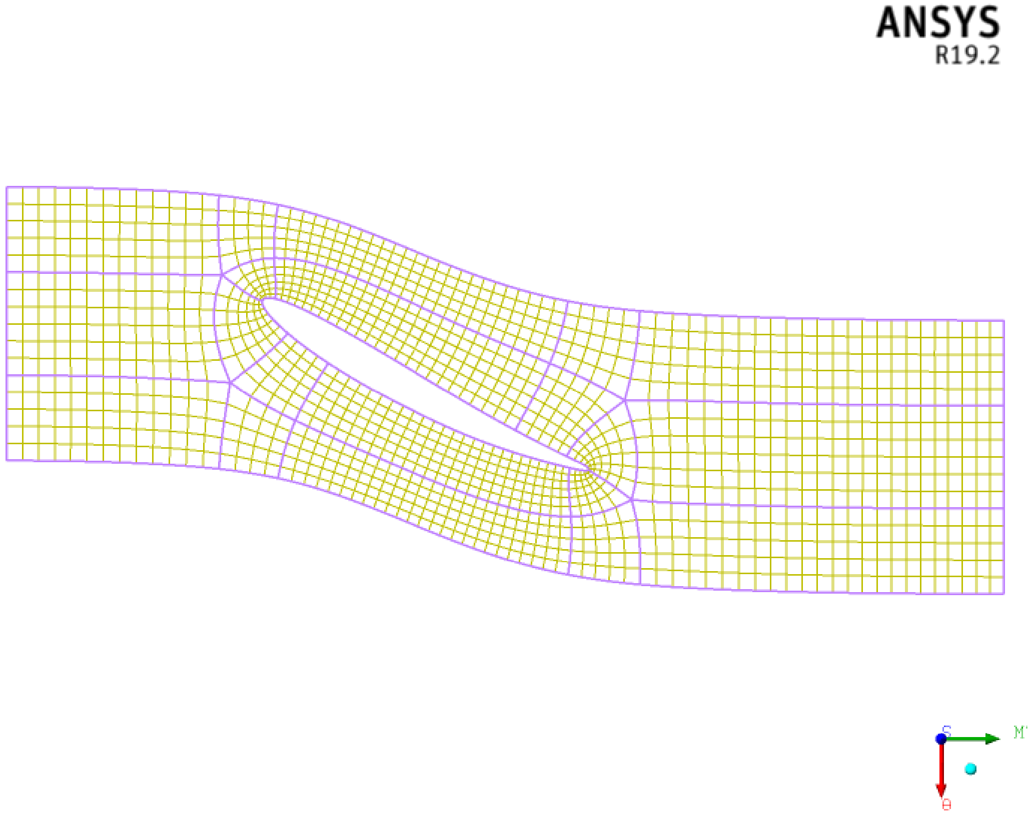

Figure 5.2: *Mesh topology layer at normalized span 0.152.*

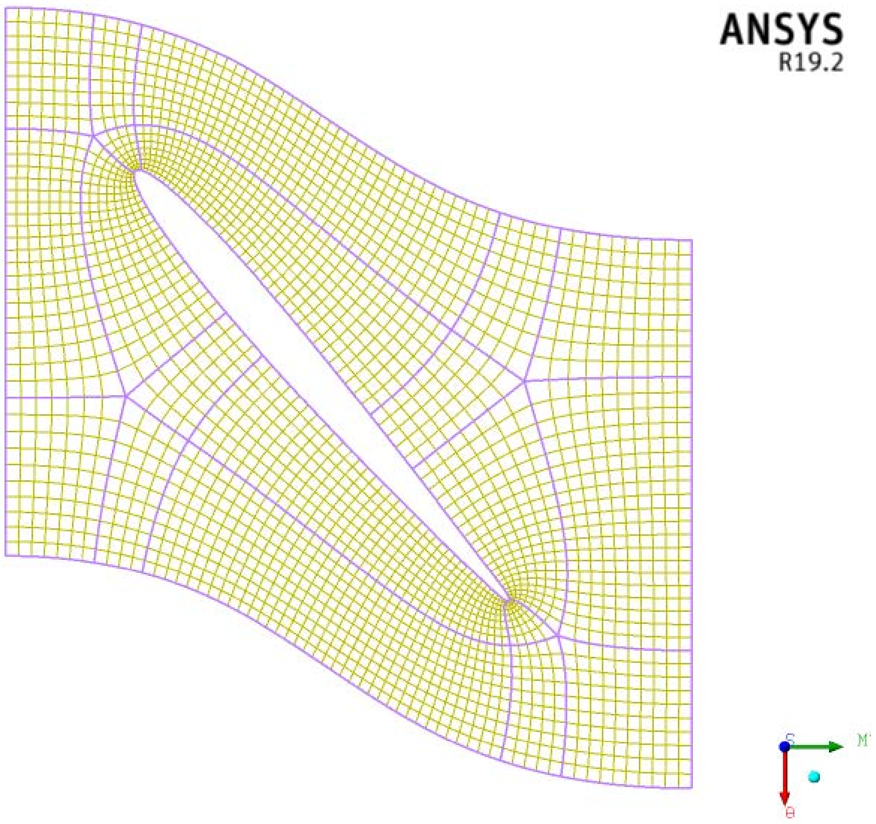

Figure 5.3: *Mesh topology layer at normalized span 0.932.*

The topology generated by the software was considered suitable for each circumferential section. Six intermediate layers were generated, two of which are represented in figures 5.2 and 5.3.

A set of regions surrounding each profile can be noted. This is the zone in which boundary layer formation and growth is expected. Lighter lines constitute a further partition of each generated region. The purpose of this second subdivision is the same as the one already discussed. It can be seen that the number of sub-regions generated varies. This is done for the same aspects considered.

5.3.2 Grid Control Parameters

Main parameters chosen to grid generation are discussed below. Initial values assigned were modified so that each evaluation parameter falls within recommended ranges. In section 5.4 definitions of evaluation parameters used are given. Thus, values reported are referred to the final mesh used. This is the result of an iterative process. These values are summarized in table 5.

Total nodes number	Boundary layer control				Radial direction gridding	
	y^+	Re_l	Expansion rate		Nodes number	Expansion rate
			Minimum	Maximum		
7.5×10^5	3.0×10^1	2×10^7	1.03	1.2	5×10^1	1.4

Table 5: *Values adopted for grid generation.*

First of all, the total number of nodes was set. This choice is the result of a trade-off between following aspects. If the quality of the generated grid is the same, then the more the nodes the better the accuracy. However, CPU time increases.

Then, boundary layer extension mesh zone was fixed. For this purpose, it was necessary to select cell number contained and the height of the first row elements adjacent to solid walls. The first parameter is a function of total nodes numbers. The height of the first row elements was kept constant along the entire extension of the solid surfaces. It was calculated by assigning two parameters: a target value for y^+ and an indicative value for the average chord Reynolds number:

$$Re_l = \frac{\rho V l_{avg}}{\mu} \tag{5.3.1}$$

To resolve the viscous sub-layer typically observable in turbulent flows, it is necessary that $y^+ < 1$. Yet, it was considered that this would have resulted in an excessive increase in the total number of nodes and so in the computational time required. For the same reason, resolution of adjacent layer, namely, buffer layer, was considered impractical. Resolving the next layer, that is the transition one, requires that $y^+ \geq 11.63$ [3]. This is the intersection value of y^+ for viscous sub-layer model and for overlap layer model of the turbulent velocity profile. To guarantee a safety margin in the use this last wall function, it was imposed that $y^+ = 30$. This last criterion is suggested by [23].

The average chord Reynolds number value was obtained by using the value of the average axial velocity upstream of the impeller. This value is the one assumed in the preliminary design, cfr. section 4.3. Values for the fluid properties used are reported in section 5.5. The arithmetic average value between single profile's chords was used as characteristic dimension.

Then, the thickness normal to the solid walls was controlled by imposing a value for the height increase of the lines next to the wall boundary. Expansion rate values were set by the software. Criteria used was to tend towards orthogonality between grid lines and the solid surfaces. This criterion ensures a gradual transition to the external region.

Finally, the radial distribution of mesh cells was controlled. This was done imposing the number of elements used and their distribution.

5.3.3 Mesh Evaluation

Mesh quality was assessed considering following parameters. Each quantifies and controls the specific phenomenon described. Table 6 also shows final values noticed, together with those recommended by the official software guide [24].

A. Partition errors. These errors can be detected if cells have a negative volume. Parameter *minimum volume of a cell* can be useful at this scope;

B. Cell skewness. Excessively distorted cells can lead to numerical instability. This phenomenon can compromise solution convergence. As a quantitative measure, Face Angle parameter was used. The *face angle of a cell surface that intersects a mesh node* is defined as the angle formed by the two edges that contain the node.

For simplicity lets consider a hexahedral cell. This *cell* is said *undeformed* if all face angles of the nodes belonging to it are straight. From these definitions, it can be deduced that values far from a reference are a measure of cell skewness. In the case of a hexahedron, the reference value is 90°.

For each node it was verified that its value were included between two recommended limits;

C. Aspect ratio. Cell shape is crucial for quantity value calculation and for spatial variation estimates. For the numerical results to be reliable, it is necessary that the ratios between cell dimensions be kept within acceptable values. *The edge length ratio of a node* is defined as the ratio between the maximum of the maximum length of the two edges of a surface that intersect the node and between the minimum of the same quantities.

It was checked that each node's edge length ratio was lower than the recommended limit value;

D. Expansion rate. Abrupt variations in cell extensions can lead to numerical instability. The *element volume ratio of a node* quantifies cell expansion rate. It is defined as the ratio between the maximum value of the cell volume that intersects a node and between the minimum value of the same quantity.

For each node it was verified that the element volume ratio was less than the recommended limit value;

E. Convergence speed. Mesh type influences the computational time. This can be point out using the *connectivity number of a node.* This parameter is the number of cells that intersect the node.

A high value of this parameter can affect convergence speed. If the number of iterations is fixed, this means that solution accuracy may decrease.

Control parameter	Observed values		Recommended values	
	Minimum	Maximum	Minimum	Maximum
Minimum volume [m^3]	4×10^{-15}	-	0	-
Face angle [°]	26	154	15	165
Edge length ratio	-	5.15×10^2	-	10^3
Element volume ratio	-	3.2	-	10
Connectivity number	-	10	-	10

Table 6: *Observed final values for mesh control.*

5.4 Numerical Flow Model

Main assumptions underlying the numerical model are presented below. Some of these have already been commented on in section 4.2.1.

1. Steady flow. Reynolds number is:

   $$Re = \frac{\rho V D_h}{\mu} \tag{5.4.1}$$

   where V is a characteristic velocity and D_h is the hydraulic diameter defined as:

   $$D_h = \frac{4A_c}{p} \tag{5.4.2}$$

   in which A_c is the cross-sectional area of the duct and p the wetted perimeter. Assuming the annulus as cross-sectional area gives $D_h = D_e - D_i$. Using for V the value assumed for $\overline{V}_{z1}$ in section 4.3, and for ρ and μ values of table 7, one obtains $Re = 2 \times 10^6$. Hence, flow regime is turbulent. Yet, temporal evolution of turbulent eddies was neglected using Reynolds-averaged Navier–Stokes (RANS) model.

   This hypothesis was adopted to reduce computational time. Furthermore, effects that turbulence causes on the main flow influence pump performance and efficiency. However, these are vortex-detail insensitive;

2. Turbulence model used was Menter shear stress transport (SST) $\kappa - \omega$ model [25], [26].

   This model was chosen for the following reasons. Reliable values for impeller efficiency and energy exchange require accurate prediction of flow separation. Standard turbulence models, such as $\kappa - \epsilon$ and $\kappa - \omega$ as proposed by Wilcox [27], predict delayed stall in adverse pressure gradient flows. As a result, wake features are underestimated. Thus, performance and hydraulic efficiency estimated with these models would be optimistic. Menter turbulence model was developed specifically for accurate stall prediction in adverse pressure gradient flows. A large number of studies demonstrated its predictive capabilities. Cfr. for example Bardina et al. [28];

3. Gravity force is neglected;
4. Fluid domain rotates at constant angular velocity. Its value was chosen in section 4.3;
5. Mesh is undeformable. This hypothesis can be considered rigorously satisfied for cells inside the domain. It can be considered acceptable for solid boundaries as long as materials used are sufficiently rigid to neglect deflections;
6. Adiabatic flow;
7. No-slip condition was assumed at solid boundaries. This is motivated by roughness of real solid surfaces. Fluid comes to a complete stop at the blade, hub and shroud. Strictly, fluid and wall velocities are equal at solid boundaries;
8. All solid surfaces are supposed perfectly smooth. This is a simplification, since roughness effects on turbulence are neglected;
9. Flow is incompressible and hence subsonic. Indeed, Mach number is below the limit value of 0.3 [29]. Hence, compressibility effects are forsaken;
10. Isothermal flow. This is commonly adopted in hydraulic flow problems. The reason lies in the following experimental observation. Temperature variation undergone by the fluid during its compression or expansion is negligible [30];

11. Flow is periodic in a tangential direction. The period is given by the (5.2.1);

12. Tangential component of absolute fluid velocity at the impeller inlet is assumed to be zero;

13. Radial component of absolute fluid velocity at the inflow is assumed to be zero.

5.5 Fluid Model Definition

Relevant hypotheses regarding the model of fluid used are examined below.

1. Fluid is composed of a single phase consisting of pure water. This is an acceptable simplification for the purposes set;

2. Fluid is in the liquid state of aggregation. From what was set in the theoretical model, it can be considered that in the design conditions cavitation is absent;

3. Fluid is modeled as a continuous. The basis for this is the nature of the experimental observations made. In facts, these are made on a macroscopic scale. This is due to performances of instruments used, which are very limited about atomic distances and time scales. Therefore, in the definition of the macroscopic quantities concepts of spatial and temporal mean of particle quantities are implicitly present. In order for the hypothesis to be allowable, two conditions must be met.

   A. An observed subsystem must be large enough to contain an adequate number of particles. In this way, it can be assumed that measurements made are statistics of atomic properties. This condition is often formulated as $Kn \ll 1$, where Kn is the Knudsen number, defined as:

$$Kn = \frac{\lambda}{L} \tag{5.5.1}$$

where λ is particle mean free path length[1] and L is a representative length scale of the problem. Since λ is of Å order and L of m order, this condition is verified;

B. The volume of the observed subsystem is small compared to the characteristic dimensions of the entire system;

4. Fluid is isotropic. As far as mechanical effects are concerned, this hypothesis can be assumed. Indeed, in a liquid the intermolecular interaction forces allow relative motion of particles. Since this is random in nature, mechanical actions are transmitted equally in all directions;

5. Fluid is homogeneous. This is legitimate, since molecular composition and nano structure of the fluid can be assumed invariant.

Values for physical properties used are those contained in the CFX-Pre software libraries. Values for relevant properties are summarized in the following table.

5.6 Boundary Conditions, Initialization and Solver Control

Boundary Conditions. Because of the hypotheses set in section 5.4, following boundary conditions are fixed.

---

[1] More properly, because of hypotesis 2, λ is the average distance between neighboring molecules.

Symbol	Value	Unit
ρ	997	$\mathrm{kg/m^3}$
μ	8.90×10^{-4}	Pa s
T	25	°C
a	1.50×10^{3}	m/s
p_{atm}	1.01×10^{5}	Pa
p_v	2.34×10^{3}	Pa

Table 7: *Main fluid properties used in numerical model.*

1. For a fixed observer fluid velocity vector at the solid walls is equal to the velocity at the wall. This results from hypothesis 7 of section 5.4;
2. Fluid temperature is constant everywhere. This follows from hypothesis 10 ibidem;
3. Fluid mass density is constant everywhere. This comes from hypothesis 9 and 10 ibidem.

To obtain in-design information, absolute velocity vector was assigned at the inflow. Uniform velocity distribution was assumed. The simplification that derives has already been discussed in section 5.2. Because of absence of data regarding inlet turbulence, the recommended ratio $\mu_t/\mu = 10$ was assumed.

For the same reason, mass flow rate was imposed at the outflow. Values for inlet velocity and flow rate were set equal to that determined in the preliminary design, cfr. table 2 of section 4.3. Using the expression:

$$\dot{m}_n = \frac{1}{N_b}\rho\overline{V}_{z1}\frac{\pi}{4}(D_e^2 - D_i^2) \tag{5.6.1}$$

it was obtain: $\dot{m}_n = 8.09 \times 10^2 \mathrm{kg/s}$.

Initialization. If initial values are representative of the real flux, then computational time can be reduced. Moreover, reliability of the solution increases and numerical instability risks decrease. This fact is particularly important if complex phenomena or unconventional fluids are modeled. In this case, initial values for velocity and static pressure were attributed following a one-dimensional and linear flow prediction model. From boundary conditions set, the software generated two points. These represents flow conditions at the inflow and at the outflow. Similarly, CFX then calculated velocity vector and static pressure at these points. For each section normal to the flow, values calculated ware assumed identical.

Solver Control. Main settings used for CFX are summarized in table 8.

Advection scheme	Maximum iterations number	Convergence criteria	
		Residual type	Residual target
Upwind	10^3	RMS	10^{-6}

Table 8: *Main solver settings employed in numerical model.*

The upwind advection scheme was adopted. Its accuracy is limited to the first order. Therefore, it is not recommended for results. Yet, it limits computational time and at the same time increase numerical stability. These factors were considered crucial in choosing the discretization scheme.

5.7 Results Discussion

Relevant results obtained from the numerical model are summarized in table 9. If an expression is provided, then numerical model value was calculated so. Otherwise, it was computed using the user interface of the CFD-Post software. Theoretical model values stem from the procedure analyzed in section 4.3. Relative error expression used is:

$$e_r = \frac{X_t - X_n}{X_n} \tag{5.7.1}$$

where e_r is the relative error, X_t the generic parameter as calculated from theoretical model and X_n the numerical one.

Results compatibility was attributed for relative errors less than 5%. This criterion is subjective. Strictly, this does not imply that values of the two models are compatible. Indeed, uncertainty analysis of both models would be necessary for a rigorous assessment. In this work, conceptual errors related to the setting of the two models were identified. For this purpose, the criterion adopted was considered acceptable.

The following can be observed from the table.

1. The quantities imposed as boundary conditions are mutually compatible.

   This fact can be explained as follows. Imposed boundary conditions values were assumed to be equal to those found in the preliminary design stage. In particular, axial absolute velocity value at the inflow was assumed to be equal to that given as input to the method of section 4.3. Moreover, volumetric flow rate value was deduced from the latter and from geometry using continuity, see figure 4.4 of section 4.3. Thus, imposed boundary conditions can be considered coherent with each other;

2. Flow coefficient values are compatible.

   This can be justified by observing that this quantity was computed as function of $\overline{V}_{z1}$ and U_e. $\overline{V}_{z1}$ is compatible with the theoretical model

Parameter	Unit	Values		Relative error [%]	Expression (numerical)
		Theoretical	Numerical		
g	m/s^2	9.81		-	-
ρ	kg/m^3	997		-	-
D_e	dm	0.83		-	-
ω	rad/s	419		-	-
$Q_{v,n}$	m^3/s	7.10×10^{-1}	7.09×10^{-1}	0.5	-
$\overline{V}_{z1}$	m/s	78	88	0	-
$\overline{V}_{\theta 1}$	m/s	0	-7.6×10^{-3}	-	-
$\overline{V}_{r1}$	m/s	0	1.1×10^{-3}	-	-
$\overline{q}_1$	bar	6.61	7.61	0	$\frac{1}{2}\rho(\overline{V_{z1}^2 + V_{\theta 1}^2 + V_{r1}^2})$
$\overline{p}_1$	bar	-	0.91	-	-
$\overline{p}_1^0$	bar	-	5.52	-	$\overline{p}_1 + \overline{q}_1$
$\overline{V}_{z2}$	m/s	15	14.2	-1	-
$\overline{V}_{\theta 2}$	m/s	-	-5.2	-	-
$\overline{V}_{r2}$	m/s	0	7.19×10^{-3}	-	-
$\overline{q}_2$	bar	-	1.65	-	$\frac{1}{2}\rho(\overline{V_{z2}^2 + V_{\theta 2}^2 + V_{r2}^2})$
$\overline{p}_2$	bar	-	2.67	-	-
$\overline{p}_2^0$	bar	-	7.22	-	$\overline{p}_2 + \overline{q}_2$
h	m	6.1	19	-76	$\dfrac{\overline{p}_2^0 - \overline{p}_1^0}{\rho g}$
$\overline{r_1 V_{\theta 1}}$	m^2/s	0	-6.3×10^{-4}	-	-
$\overline{r_2 V_{\theta 2}}$	m^2/s	-	-4.87×10^{-1}	-	-
h_t	m	15.1	27	-75	$\dfrac{\omega(\lvert\overline{r_2 V_{\theta 2}}\rvert - \overline{r_1 V_{\theta 1}})}{g}$
η_{id}	-	0.5	0.7	0	h/h_t
ϕ	-	0.37	0.369	0.1	$\overline{V}_{z1}/(\omega \frac{D_e}{2})$
ψ	-	0.127	0.22	-77	$gh/(\omega \frac{D_e}{2})^2$
ψ_t	-	0.134	0.24	-76	$gh_t/(\omega \frac{D_e}{2})^2$
N_s	-	14	4	189	$\omega\sqrt{Q_{v,n}}/(gh)^{0.75}$

Table 9: *Theoretical and numerical model results comparison.*

For relative error e_r definition, see (5.7.1).

as discussed in the previous point. U_e can be expressed as a univocal function of impeller geometry and angular velocity. These last quantities were imposed in the numerical model. Further, values adopted are identical to the ones assigned in the theoretical model. Therefore, thesis follows;

3. Impeller specific work of the numerical model is four times greater than the theoretical model value.

   This discrepancy can be explained by the following argument. For simplicity sake, let us adopt a one-dimensional model. Then, from velocity triangle relationships:

   $$h_t = U_2 V_{\theta 2} = U_2 (U_2 - \frac{V_{z2}}{\tan \beta_2}) \tag{5.7.2}$$

   As seen, U_2 and V_{z2} are compatible with the theoretical model. From equation (4.4.6) of section4.4, β_2 can be expressed as unique function of blade geometry, inlet flow angle and incidence. If external devices such as inlet guide vanes are excluded, then $V_{\theta 1} = 0$. Axial absolute velocity at the inflow is compatible. Furthermore, $\tan \beta_1 = V_{z1}/U_1$. Then, it follows that β_1 is in turn compatible with theoretical model. Blade geometry is identical to that determined by the theoretical model. Besides, incidence values assigned are positive, cfr. table 3. Thus, it follows that β_2 values increase because of the imposition on i. β_2 values of the theoretical model do not include later modification of incidence. Then, differences on h_t values are evident;

4. Hydraulic efficiency values are compatible each other.

   Criterion by which this value was assigned in the preliminary design was concealed. Then, it is impossible to prove if assumptions that led to this value were verified in the numerical model;

5. Incompatibilities on h, ψ, ψ_t and N_s can be justified on what has been developed so far;

6. Absolute upstream static pressure value relative to theoretical model is not given.

   In fact, based solely on data reported in section 4.3, this value is undefined. This fact can be inferred by noting that the radial equilibrium equation (4.2.1) is a differential relation. Thus, deduction of pressure by integration requires a constant to be fixed;

7. Static pressure value computed from numerical model is lower than atmospheric value. This fact is in contrast with actual impeller operating conditions.

   In fact, the waterjet in question works with an intake. This is located upstream with respect to the impeller to improve its performance. In fact, one of inlet tasks is to ensure that flow upstream of the impeller possesses an absolute velocity value as close as possible to design one. In fact, its performance and efficiency are greatest for this value. Free-stream velocity value at the waterjet design point is greater than impeller inlet velocity, see next section. Moreover, flow is subsonic. From these facts, it can be argued that the intake realizes it purpose if it diffuses the incoming fluid. If waterjet design point is the same as that of the impeller, then diffusion occurs efficiently. Hence, deceleration of the flow is accompanied by a static pressure rise. If jet axis is close to the free surface of water, then free-stream static pressure can be assumed equal to atmospheric pressure. Thus, it is concluded that the numerical model value is misleading.

8. The fact that a lower-than-atmosphere pressure value was obtained is

due to an improper choice of boundary conditions.

In fact, from continuity point of view, these define the physical problem. Yet, imposing throughflow velocity and volumetric flow rate at the same time is a sufficient but not necessary condition. In fact, under hypothesis 9 of section 5.4, flow can be assumed incompressible. Therefore, providing a single quantity between velocity and flow rate is sufficient. Indeed, the one left is determined imposing continuity.

Boundary conditions chosen make numerical flow model under-specified from momentum point of view.

This fact can be proved following the same argument made at previous point. Equivalently, it can be asserted that data contained in boundary conditions are insufficient to observe the modeled physical phenomenon;

9. Values of absolute tangential velocity and angular momentum at the inlet are lower than threshold. Thus, hypothesis 12 of section 5.4 is satisfied. Same criterion leads to assert that hypothesis 13 ibidem is also verified. The same argument can also be applied to $\overline{V}_{r2}$. Hence, outside of the blade-to-blade duct, stream surfaces can be assumed cylindrical.

The fact that inlet average static pressure is sub-atmospheric has led to following thought. It was considered if areas with lower-than-saturated steam pressure at the flow temperature could exist. Such a region was actually found. It can be observed in figure 5.4.

From this fact, it was concluded that hypothesis 2 of section 5.5 has not been verified. However, it is believed that this fact prevents one from concluding that pump cavitation behavior is bad. This statement may be

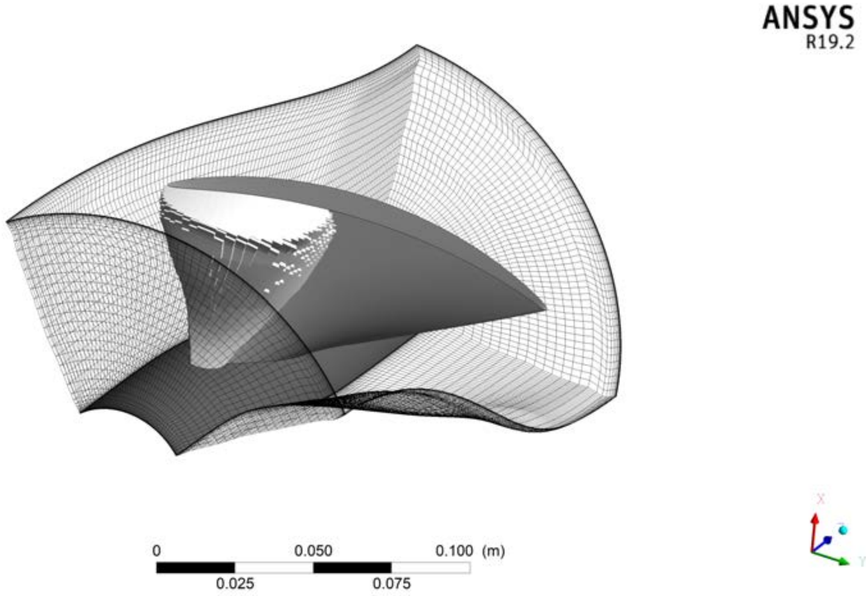

Figure 5.4: *Cavitation bubble identified by numerical model.*

This region was identified by imposing $p \leq p_v$. It can be argued that cavitating volume extends in the suction side of the blade. Also, near the shroud this phenomenon is broader.

justified by the considerations developed in point 6. Furthermore, present argument corroborates the same thesis.

Impeller $NPSH$ is:

$$NPSH = \frac{p_1 - p_v}{\rho g} + \frac{\overline{V}_{z1}^2}{2g} \tag{5.7.3}$$

If cavitation occurs, then $NPSH \leq NPSH_r$, where $NPSH_r$ is the total fluid head *required* for cavitation. At this value of $NPSH$ critical conditions are verified, namely incipient cavitation takes place. This means that in the lowest pressure point of the impeller $p = p_v$. Fluid $NPSH_r$ can be expressed as a function of impeller geometry and operating conditions [18]. In fact, for an axial flow pump the following applies:

$$NPSH_r = (1 + \lambda_m)\frac{(V_{z1}^*)^2}{2g} + \lambda_w \frac{(W_1^*)^2}{2g} \tag{5.7.4}$$

where λ_m is a loss coefficient, λ_w a blade load factor and superscript * denotes minimum pressure point. This expression can be approximated as:

$$NPSH_r \approx (1+0.05)\frac{\overline{V}_{z1}^2}{2g} + 0.85\overline{C}_L\frac{\overline{W}_{\infty}^2}{2g} \tag{5.7.5}$$

Entering preliminary design values for average velocities, one has $NPSH_r =$ 24m. For a waterjet, in-design energy *available* $NPSH_a$ is [4]:

$$NPSH_a = \frac{p_{atm}-p_v}{\rho g} + \frac{V_{\infty}^2}{2g} - h_f \tag{5.7.6}$$

in which V_{∞} is the free-stream velocity and h_f is the friction head between undisturbed flow section and impeller inlet. These losses can be estimated as:

$$h_f = \frac{e_1 - e_{\infty}}{g} = -\frac{\overline{p}_1 - \overline{p}_{1d}}{\rho g} + \frac{\overline{V}_{1d}^2 - \overline{V}_1^2}{2g} = -C_{PR}\frac{(\overline{V}_{1d})^2}{2g} + \frac{\overline{V}_{1d}^2 - \overline{V}_1^2}{2g} \tag{5.7.7}$$

where $\overline{p}_{1d}$ is the average absolute pressure and $\overline{V}_{1d}$ the average velocity at diffuser inlet and C_{PR} its static pressure recovery coefficient. Using continuity for $\overline{V}_{1d}$ and next section numerical values: $h_f = 3$m and so $NPSH_a =$ 3.3×10^2m. $NPSH_a$ is greater than $NPSH_r$. Therefore, at the design point cavitation is absent.

From the developed discussion, these facts emerge.

A. Impeller energy-exchange quantities are incompatible. This is due to *a posteriori* adjustment made on incidence in the preliminary design. As seen in section 4.4, to obtain compatibility, a revision of mean camber line part is necessary. In this regard, it is noted that coherence for theoretical model can be obtained in different ways;

B. Numerical model fails to predict impeller actual in-design operating conditions. This fact results from an improper choice of the boundary conditions. This lack could be solved by assigning a condition to define continuity and the remainder for force balance resolution.

In order to obtain the missing information relative to point **B**, an analysis of the process operated by the diffuser is necessary. This survey is proposed in following section.

6 Diffuser Flow Analysis

6.1 Introduction

Numerical model results discussion of previous section highlighted its unreliability. In fact, according to this model static pressure value at the impeller inflow is lower than the atmospheric value. This fact was considered unacceptable. Indeed, because of flow diffusion inside and outside the intake, static pressure at impeller inflow is expected higher than atmospheric. Furthermore, this model detected a cavitating area near the blade suction side. From preliminary design data, it has been shown that this phenomenon is unexpected.

Both these issues can be solved if boundary conditions are modified to take into account diffusive processes. This change is necessary for the numerical model to be representative of the observed physical phenomenon.

At this aim, in present section a survey of flows inside and outside the diffuser is presented. The goal is to develop a simple-enough theoretical model allowing a quick estimate of the static pressure built upstream of the impeller. Fundamental conservation principles of fluid mechanics and aeronautics theoretical and experimental data are used. Care was given to the discussion of a proper use of aeronautical results. Simplifying hypotheses validity is treated in details.

Then, acceptability of the results obtained is debated. Data obtained in this way are used to adapt boundary conditions of the initial numerical model. Finally, results are discussed and compared with those presented in section 3.

6.2 Conservation Principles for Internal Flow

By examining diffuser internal flow, a model can be developed. It attains data needed for estimating the static pressure value downstream of the diffuser. This tool is summed up by the application of fluid mechanics fundamental principles expressed in a simple analytical form. Yet, their validity relies on a set of assumptions relating to the process considered.

For the model to produce suitable results, hypotheses must be acceptable. Thus, once again, care is given to the discussion of their properness. Some discussions have already been debated in sections 4.2.1, 5.4 and 5.5. Therefore, reader is referred to these, where comments are omitted.

Figure 6.1 shows the diffuser type used by the designer. As can be argued, a ram inlet was chosen. Relevant fluid dynamics parameters are also designated. These are: inlet diameter at the lip, called *highlight diameter* and indicated with D_{hl}, diffuser minimum and maximum inner diameters, D_{1d} and D_{2d} respectively and diffuser length N. Corresponding dimensions are summed up in table 10.

Symbol	Value
D_{hl}	0.83
D_{1d}	0.65
D_{2d}	0.83
N	1.7

Table 10: *Main diffuser dimensions.*

All values are expressed in dm.

A reference control volume is dashed. This is defined as the fluid region between diffuser inner walls, its minimum and maximum section, A_{1d} and

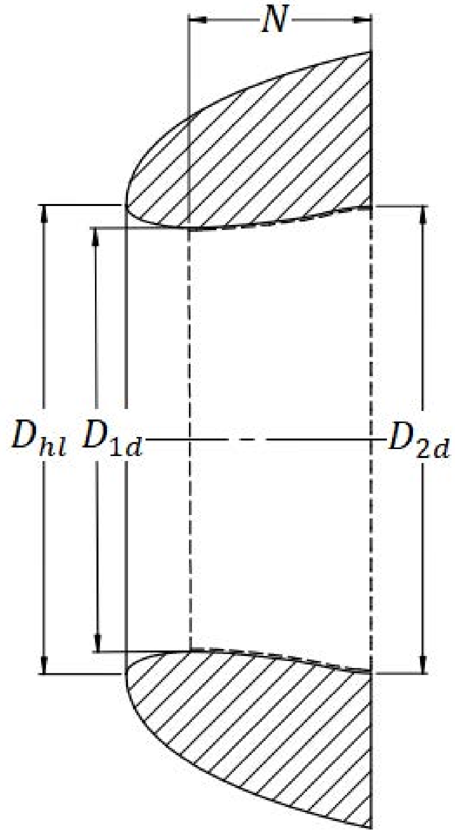

Figure 6.1: *Section view of the ram inlet adopted.*

The model is of aeronautical derivation: NACA 1-85-43.9 was used.

Meridian plan was chosen as the cutting one. In this way, diffuser internal and external shapes can be observed. Solid surfaces are hatched. Control volume considered for the analysis is dashed.

A_{2d} respectively. The latter coincides with diffuser exit section, by virtue of its diverging shape. Due to the lip between inner walls and the cowl, A_{1d} is generally placed downstream with respect to diffuser inflow section. Fluid volume selected consists of one inlet and one outlet. This is a consequence of the choice made on its definition and it is aimed to simplify equations form.

To write continuity principle, following hypotheses are placed:

1. Fluid is modeled as a continuous;

2. Steady flow. This hypothesis is legitimate when the reference frame assumed is stationary with respect to the waterjet.

   A quiescent observer with respect to the waterjet will measure a certain value for the freestream velocity. If this value is equal to the vessel speed as measured by an Earth-fixed observer, then the same phenomenon is observed. This is guaranteed by the principle of inverted flows, which is a consequence of the first principle of dynamics [31].

   Besides, unsteadiness and nonuniformity of the fluid upstream and past the waterjet must be neglected. This condition is an acceptable simplification for the purposes set [32];

3. Incompressible flow;

4. Flow is supposed to be uniform in A_{1d} and in A_{2d}. This is a major simplification. Indeed, in the real flow all fluid properties vary from point to point. Yet, if the flow is turbulent and diffuser inner walls variation is moderate, then this approximation is acceptable.

   In fact, let us consider turbulent flows inside pipes. Typically, observed velocity profiles are flat. So, average velocity value can be assumed as representative of the entire section. This fact is owned to turbulence action. Indeed, it enhances momentum transport within the fluid. For this reason, the same behavior is to be expected within diverging ducts. Instead, inner walls gradual variation ensures that boundary layer remains attached, viz. stall is prevented. Indeed, boundary layer detachment would result in wakes. In these regions, velocity is remarkable lower.

In conclusion, if these conditions are satisfied, then average velocity is representative of the entire flow section, except for a thin region close to solid walls.

If hypotheses 1-4 are true, then mass conservation principle at A_{1d} is written as:

$$\dot{m} = \rho V_{1d} A_{1d} \tag{6.2.1}$$

From which the velocity value can be obtained:

$$V_{1d} = \frac{\dot{m}}{\rho A_{1d}} = \frac{Q_v}{\frac{\pi}{4} D_{1d}^2} \tag{6.2.2}$$

Using data of tables 2 and 10, it is found that $V_{1d} = 20.5\text{m/s}$.

Besides, these extra hypotheses are put to write conservation energy principle in a simple form:

5. Fluid geodetic height variations are ignored. This is proper for the waterjet in question. In fact, it employs a ram diffuser. Its axis coincides with that of the impeller;

6. Adiabatic flow. As was seen for the impeller at section 4.2.1, flow can be considered incompressible. Thus, even in this case the condition is satisfied;

7. Isothermal flow.

Therefore, the first law of thermodynamics becomes:

$$\frac{p_{2d}}{\rho} + \frac{V_{2d}^2}{2} - (\frac{p_{1d}}{\rho} + \frac{V_{1d}^2}{2}) + e_{2d} - e_{1d} = 0 \tag{6.2.3}$$

From which internal energy increase can be deduced:

$$e_{2d} - e_{1d} = -\frac{(p_{2d} - p_{1d})}{\rho} + \frac{V_{1d}^2 - V_{2d}^2}{2} \tag{6.2.4}$$

This increase is equal to the decrease in thermodynamic work that the system could deliver on the surroundings. Thus, this variation can be read as energy dissipation.

In details, internal energy increase is shown as thermal energy increase. Since fluid state of aggregation remains unchanged, this increase enhances its sensible energy. As a result, an increase in fluid temperature is expected. Apparently, this is in conflict with hypothesis 7. Nevertheless, in-design energy dissipation is contained. Thus, as far as temperature effects are concerned, the resulting variation can be neglected [3], [30].

From equation (6.2.4), it can be noted that $e_{2d} - e_{1d}$ can be determined once static pressure rise operated by the diffuser is known. This can be estimated using experimental results related to subsonic diffusers. The procedure is described in detail in the next section.

6.3 Static Pressure Rise Estimate

As described in figure 6.1, the designer used the model NACA 1-85-43.9. The reason underlying this choice is its suitability for low subsonic flows. In fact, a blunt cowl lip can be seen from the figure. This results in a gradual variation of diffuser internal geometry. In turn, this reduces stall risk in the most critical part, viz. at the beginning of the divergent portion.

This intake is of aeronautical derivation. Experience gained in this sector allows diffuser performance evaluation at the design point as a function of its geometry. Yet, it should be noted that these results are related to a distinct physical phenomenon, because of the different fluid involved. Thus, the appropriateness of usage of such data must be discussed.

This problem was addressed in the following terms. First, a set of relevant aspects inherent to diffuser performance were identified. Then, conditions for their flow similarity in marine applications were discussed. This survey is summed up in the following points.

A. Major losses. Due to viscosity, part of fluid macroscopic kinetic energy is converted into internal energy. In particular, this transformation results in a sensible energy increase. Thus, diffuser is unable to generate a pure static pressure rise. Therefore, degradation energy process takes place. This involves frictional stresses exerted by diffuser inner walls on the adjacent fluid. In addition, viscous and turbulent shear stresses exchanged between adjacent fluid elements are implied. Yet, at the design point, energy degradation effects of the latter are negligible if compared to those produced by the former. In fact, in this condition fluid velocity gradients are larger near the walls. For a fully developed flow, wall friction can be expressed as:

$$\tau_w = f(\rho, \mu, V, D, \varepsilon) \tag{6.3.1}$$

where τ_w is wall shear stress, ρ the fluid density, μ fluid dynamic viscosity, V fluid characteristic speed, D a representative diffuser diameter and ε diffuser average wall roughness height. With dimensional analysis theory, it can be shown that the following functional relationship holds:

$$f = \frac{8\tau_w}{\rho V^2} = f(Re, \frac{\varepsilon}{D}) \tag{6.3.2}$$

where f is Darcy friction factor. As far as water is concerned, above a certain value of the Reynolds number f is independent of Re, [33]. Hence, wall friction phenomenon can be assumed similar once ε/D ratios are equal. If this is true, then the relative thickness of the boundary layer is expected to be the same. In fact, its extension depends on the magnitude of velocity gradients within it. In turn, this depends on flow regime and wall shear stresses. As these factors are similar, thesis follows.

Yet, fully developed turbulent flow is an approximation. In fact, boundary layer establishment and growth are associated with a gradual decrease in wall shear stresses. When a constant value is reached, then fully turbulent flow is established. The extension of the region in which these phenomena take place is called *entry region.* An estimate of its length is given by the following [34]:

$$L_h = 1.359 Re^{0.25} D \tag{6.3.3}$$

Inserting fluid data of table 7, using $V = V_{1d}$ and taking the arithmetic mean value between D_{1d} and D_{2d} for D, it is found that $L_h = 10\text{m}$.

B. Minor losses. For the diffuser of figure 6.1, these losses are due to the detachment of the boundary layer from solid walls. This phenomenon is promoted by an adverse pressure gradient. Yet, in in-design condition, diffuser geometry is such as to ensure that the boundary layer remains attached. Then, this phenomenon is absent;

C. Diffuser geometry. Its section shape and its axis curvature affect the extent and type of secondary flows. Together with exit-to-inlet area ratio and its axial length influence the flow regime, too [35]. The entity of major and minor losses are influenced, as well. In fact, these features determine diffuser divergence angle.

If all the above conditions are met, then aeronautical results usage was considered legitimate.

The intake geometry of figure 6.1 was considered as conical. This represents a further approximation. Yet, it was considered appropriate for a first estimate of static pressure value.

Thus, $p_{2d} - p_{1d}$ increment was estimated using Sovran and Klomp chart. This is plotted in figure 6.2.

This graph summarizes experimental test results relating to in-design performance of a conical subsonic diffuser as a function of its geometry. *Static pressure recovery coefficient* contours is chosen as performance parameter. It is defined as:

$$C_{PR} = \frac{p_{2d} - p_{1d}}{q_{1d}} = \frac{p_{2d} - p_{1d}}{\frac{1}{2}\rho V_{1d}^2} \tag{6.3.4}$$

where q_{1d} is the dynamic pressure at the diffuser inlet.

It can be noted that this parameter is an index of the amount of natural diffusion undergone by the fluid. In fact, for a given vessel speed the dynamic pressure upstream of the diffuser is constant. Then, an increase of C_{PR} results in a pressure rise. With upstream pressure being the same, downstream pressure is greater. Hence, natural diffusion is more effective.

From geometric data of table 10, in-design C_{PR} value of 0.2 was read in figure 6.2. Since $V_{1d} = 20.5\text{m/s}$, a diffuser pressure rise of $\Delta p_d = p_{2d} - p_{1d} = 42\text{kPa}$ was obtained. Entering this in (6.2.4), an estimate of the hydrodynamic losses that take place inside the diffuser was found to be: $e_{2d} - e_{1d} = 29\text{J/kg}$, with $V_{2d} = Q_v/A_{2d} = (1 - \frac{1}{(D_e/D_i)^2})\overline{V}_{z1} = 16.6\text{m/s}$.

6.4 Captured Streamtube Flow Analysis

Mere diffuser internal flow analysis is insufficient to estimate downstream static pressure. For this purpose, further data can be gained reviewing waterjet external flow.

Similarly to section 6.2, results are summed up in a set of equations. Its suitability stems from model assumptions compliance. These are discussed below, after system definition.

Figure 6.3 shows a section of the control volume considered. This is

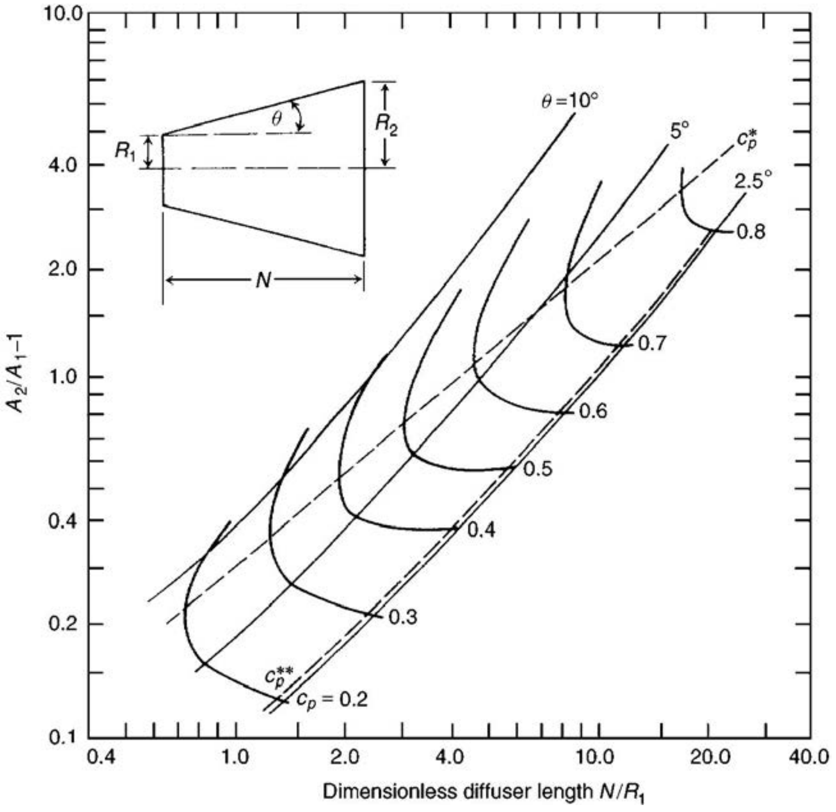

Figure 6.2: *Static pressure recovery coefficient contours as a function of geometry for in-design operation of a conical diffuser [6].*

A sufficiently high Re is assumed, to ensure a turbulent boundary layer at the inlet. In-design condition is expressed in terms of relative boundary layer thickness. Indeed, this chart is valid for a prescribed displacement thickness. This is formulated as: $B_1 = A_{B,1}/A_1 \sim 2\%$, *where* B_1 *is the area blockage parameter at diffuser inlet,* $A_{B,1} = \iint_{A_1}(1 - u/u_e)dA$ *is the inlet blocked area and* A_1 *the inflow cross-sectional area. Of the four geometric parameter sketched, only three are independent. Indeed:* $\tan\theta = (R_2 - R_1)/N$. *Hence, conical diffuser shape is defined once two dimensionless ratios are given. Thus, knowing* N/R_1 *and* $A_2/A_1 - 1$, *it is possible to find diffuser* C_p.

This chart can also be used for design purposes. Indeed, for a prescribed N/R_1 *or* $A_2/A_1 - 1$, C_p^* *and* C_p^{**} *define that diffuser area ratio and non-dimensional length value, respectively, producing the maximum static pressure recovery.*

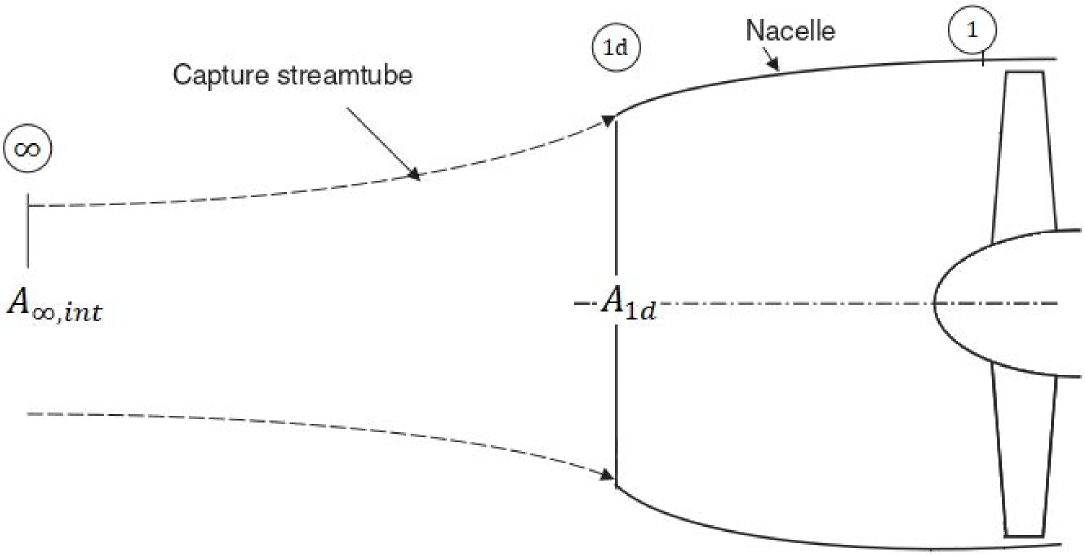

Figure 6.3: *Fluid control volume for captured streamtube analysis. [7].* *In-design geometry of the captured streamtube is sketched. Stagnation circumference is supposed to coincide with* A_{1d}*. Referring to figure 6.1, it can be argued that 2D corresponding stagnation points are located well-below the highlight section points. This approximation is acceptable for high-speed operation [9].*

bounded by the edges of internal flow dividing stream surface. The corresponding streamtube is called *captured streamtube*. Control volume end sections $A_{\infty,int}$ and A_{1d} are normal to diffuser axis. In the waterjet under analysis, this axis is the same as the impeller one. In $A_{\infty,int}$ the flow is assumed undisturbed, while A_{1d} coincides with diffuser minimum section. In the figure, the cowl lip is omitted. Due to these choices, control volume has only one inlet and one outlet. This fact simplifies equation forms.

Assumptions relating to continuity equation are identical to those commented in section 6.2, with a proper extension of symbols. If these are true, then continuity is written as:

$$\dot{m} = \rho V_\infty A_{\infty,int} \tag{6.4.1}$$

In which both V_∞ and $A_{\infty,int}$ are unknowns.

Energy conservation principle relies on further hypotheses 5, 6, 7 of section 6.2. Furthermore, external flow between $A_{\infty,int}$ and A_{1d} is assumed isentropic. This is an acceptable simplification. In fact, losses that occur therein are negligible as compared to those between A_{1d} and A_{2d} [7]. Because of these assumptions, the first law of thermodynamics is formally equal to the second law of dynamics. Bernoulli's equation is obtained:

$$p_\infty + \frac{\rho V_\infty^2}{2} = p_{1d} + \frac{\rho V_{1d}^2}{2} \tag{6.4.2}$$

In equation (6.4.2), V_∞ and p_{1d} are unknowns.

Another relationship between unknowns can be found as follows. Referring to the control volume as defined previously, let us substitute the A_{1d} end section with A_{2d}. Using the same hypotheses, the first principle of thermodynamics is written as:

$$\frac{p_{2d}}{\rho} + \frac{V_{2d}^2}{2} - (\frac{p_\infty}{\rho} + \frac{V_\infty^2}{2}) + e_{2d} - e_{1d} = 0 \tag{6.4.3}$$

with $e_{2d} - e_\infty = e_{2d} - e_{1d}$ for the last assumption. In this equation, p_{2d} and V_∞ are unknowns.

The system of equations (6.4.1), (6.4.2), (6.4.3) is insufficient to find the four unknowns V_∞, $A_{\infty,int}$, p_{1d} and p_{2d}. This issue can be solved by developing another model for the external waterjet flow. This model leads to an estimate of $A_{\infty,int}$ as a function of forebody intake geometry. Details are given in next section.

6.5 An External Flow Model

In section 3.2 it was seen that an extra task of ram-type intakes is drag containment. Actually, all the components exposed to external flow share this function.

In addition to the diffuser, also the whole waterjet fairing shape was borrowed from aeronautics. Details are concealed. Yet, it is known that a solution for low subsonic applications was employed. Its shape is represented in figure 6.4. Two useful geometrical parameters are indicated. D_m designates fairing maximum diameter and l_{max} defines the distance along the fairing axis between A_{hl} and A_m. Their values are known and reported in table 11.

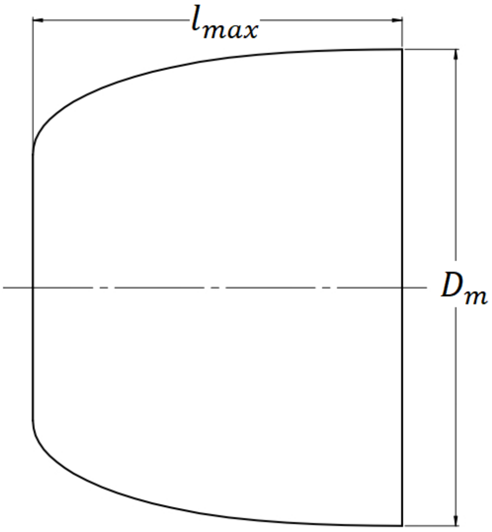

Figure 6.4: *Outline of the forebody intake.*
Waterjet fairing up to maximum cross-section is sketched. Parameters D_m and l_{max} are reported. These are of interest for an estimate of $A_{\infty,int}$.

Then, aeronautics experience in external flows was considered appealing. Once again, for these results to be exploitable, the problem of the different phenomenon studied must be consider.

For external flows over a streamlined body, resultant of normal and shear stresses continuously distributed over its surface are of interest. These can be reduced to a single resultant force and moment. The latter is considered

Symbol	Value
D_m	4.3
l_{max}	1.5

Table 11: *Values of fairing parameters of interest for external flow analysis. All values are expressed in* dm.

applied in a reference point, called center of moments.

In general, each has three component. Referring to the so-called wind coordinate system, force components are said drag, lift and side force. Instead, moment components are said rolling, yawing and pitching. Relative magnitude of these components depends on body geometry and its orientation relative to flow [31]. If an axisymmetric body is considered and straight and unaccelerated conditions are examined, i.e. with slideslip angle equal to zero, then the only relevant force components are lift and drag [31]. These assumptions are proper for waterjet in-design analysis. Concerning moment components, it turns out that only pitching is significant. Besides, this forces and moment system can be reduced to a single resultant if applied to its central axis. In aerodynamics, this is often called center of pressure. Thus, with these assumptions, only lift and drag components need to be considered.

Lift. Relevant parameters affecting lift force exerted on a streamlined body are fluid properties, viz. density ρ, dynamic viscosity μ and sound speed a, flow characteristics, namely freestream velocity magnitude V_∞ and the angle of attack α and body geometry, i.e. chord length l. So:

$$F_L = f(\rho, \mu, a, V_\infty, \alpha, l) \tag{6.5.1}$$

in which F_L is the lift force. Applying similitude theory, following functional relationship is obtained:

$$C_L = \frac{F_L}{\frac{1}{2}\rho V_\infty^2 A} = f(Re, M, \alpha) \tag{6.5.2}$$

where A is the planform area of the body and M Mach number. Hence, to obtain lift similarity, four conditions have to be accomplished, viz. body shape, α, Re and M must be equal. Yet, for low subsonic flows, i.e. for $M < 0.3$, compressibility effects are negligible [3]. Thus, M dependence drops. Strictly, this is a simplification. Further, if flows are supposed to be turbulent, then Re condition can be considered satisfied, even though its values are different. Of course, this is another approximation.

Drag. For low subsonic flows, discussions made on internal flow at section 6.3 can also be extended to the external one, with appropriate adaptations.

Thus, for aeronautical results to be properly used, following conditions must be accomplished:

1. Waterjet and aircraft fairing shape must be the same. This condition is necessary for geometric similarity to be absolved;

2. $M < 0.3$. This allows to neglect compressibility effects and so M dependence;

3. Turbulent flow. This is necessary for Re condition to be accomplished;

4. Incidence angle must be equal;

5. Fairing relative roughness must be the same. This guarantees that boundary layer relative thickness is the same.

If all these criteria are satisfied, aeronautical results usage was considered legitimate.

In subsonic air intakes, engine cowl drag is mainly influenced by static pressure distribution therein and around its lip. In fact, experimental investigations show that this pressure distribution is poorly affected by that inside the diffuser [9]. Then, drag phenomenon can be studied considering only the cowl and its lip.

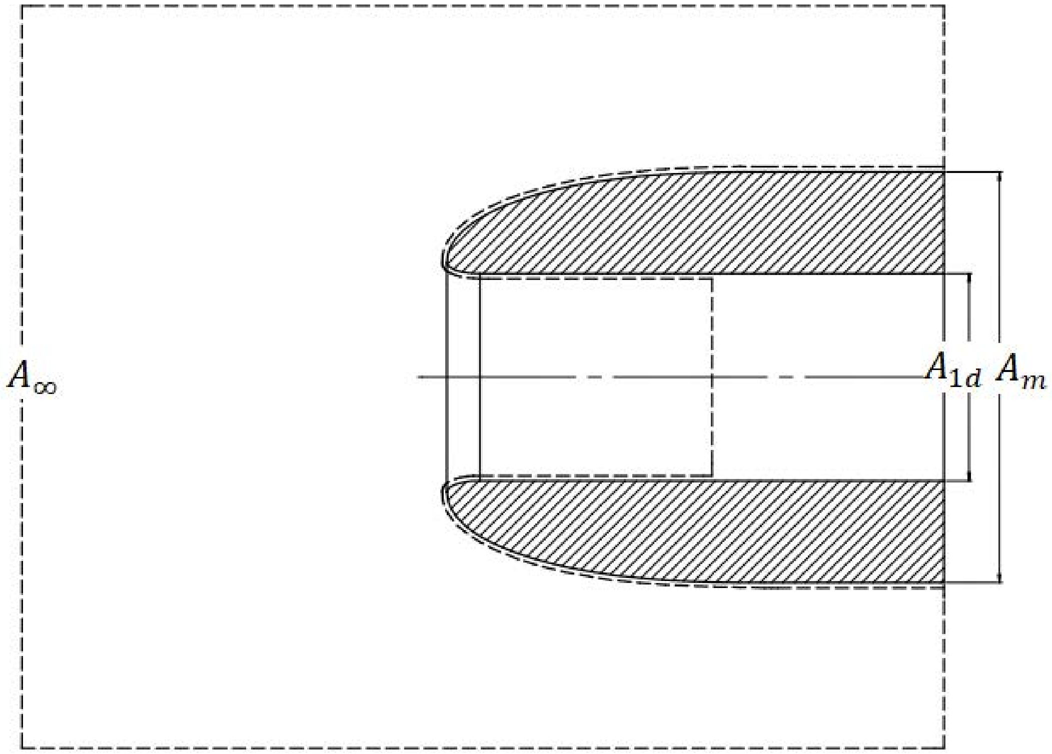

Figure 6.5: *Geometric model of the forebody intake for external flow study. Control volume considered for the analysis is dashed. Solid surfaces are hatched.*

Figure 6.5 shows a section along the meridian plane of the intake cowl model used. This is defined as follows. If A_m denotes fairing maximum frontal area, then intake shape is considered arbitrary but defined between A_{1d} and A_m. As seen, static pressure distribution influence beyond A_{1d} can be neglected. Thus, for simplicity sake, diffuser internal geometry is supposed simply cylindrical after A_{1d}. Beyond A_{1d} and A_m the nacelle is endless.

In the same figure, the control volume used is dashed. Fluid inlet section is A_∞. This area is located at enough distance from the intake so that a freestream flow can be assumed. Two outlet sections can be noted: A_{1d} for internal flow and $A_\infty - A_m$ for external flow. A_∞ extension allows assuming that in $A_\infty - A_m$ the average velocity is V_∞. External lateral surface is equal to the cylindrical lateral surface whose base is A_∞. The remaining surface is identical to the nacelle one.

To write Newton's second law along the fairing axis, hypotheses 1-5 of section 6.2 are assumed valid. In particular, hypothesis 4 is related to the inlet and outlet sections. Besides, flow between A_∞ and A_{1d} is assumed to be isentropic. This was already discussed in section 6.3. Finally incidence angle is zero. This is appropriate in waterjet regime operation.

In these hypotheses, momentum theorem becomes:

$$R_{ext} = \sum_{k=1}^{2} (\dot{m}V)_{outlet,k} - (\dot{m}V)_{inlet} \tag{6.5.3}$$

Where R_{ext} is the resultant of external forces that the surroundings exerts on the control volume. Assuming $\overrightarrow{V_\infty}$ sense as positive, from the hypotheses, it follows that:

$$p_\infty A_\infty - p_{1d}A_{1d} - p_\infty(A_\infty - A_m) - \iint_{A_n} p dA_n = \rho A_{1d}V_{1d}^2 + \rho(A_\infty - A_m)V_\infty^2 + \\ - \rho A_\infty V_\infty^2 \tag{6.5.4}$$

In the fourth term, A_n is the cowl surface area projected normally to its axis, while dA_n is its infinitesimal element. Of course: $A_n = A_m - A_{1d}$. The sense of this pressure force is assumed to be opposite to $\overrightarrow{V_\infty}$ one. This justifies its negative sign. Using continuity:

$$\rho(A_\infty - A_m)V_\infty = \rho A_\infty V_\infty - \rho A_{1d} V_{1d} \tag{6.5.5}$$

Entering the (6.5.5) in (6.5.4) and simplifying:

$$-p_{1d}A_{1d} + p_\infty A_m - \iint_{A_n} p dA_n = \rho A_{1d} V_{1d}(V_{1d} - V_\infty) \tag{6.5.6}$$

Or:

$$\iint_{A_n} p dA_n = \rho A_{1d} V_{1d}(V_\infty - V_{1d}) + p_\infty A_m - p_{1d}A_{1d} \tag{6.5.7}$$

Yet:

$$\iint_{A_n} p dA_n = \iint_{A_n} (p - p_\infty) dA_n + p_\infty(A_m - A_{1d}) \tag{6.5.8}$$

Therefore, the (6.5.7) becomes:

$$\iint_{A_n} (p - p_\infty) dA_n = \rho A_{1d} V_{1d}(V_\infty - V_{1d}) - (p_{1d} - p_\infty)A_{1d} \tag{6.5.9}$$

Since the flow between A_∞ and A_{1d} is isentropic, Bernoulli can be written:

$$p_\infty + \frac{\rho V_\infty^2}{2} = p_{1d} + \frac{\rho V_{1d}^2}{2} \tag{6.5.10}$$

from which:

$$p_{1d} - p_\infty = \frac{\rho}{2}(V_\infty^2 - V_{1d}^2) \tag{6.5.11}$$

Replacing the latter in (6.5.9) and manipulating:

$$F_z = -\iint_{A_n} (p - p_\infty) dA_n = \frac{1}{2}\rho V_\infty^2 A_{1d}\Big(1 - \frac{V_{1d}}{V_\infty}\Big)^2 \tag{6.5.12}$$

where F_z is defined as the force component parallel to V_∞ that the fluid exerts on the fairing. Because of the initial convention on the integral, F_z is considered positive if opposed to $\overrightarrow{V_\infty}$ sense. Then, from (6.5.12) it is concluded that F_z is always a thrust. This force may make an appreciable contribution to the overall thrust-drag balance [9]. In dimensionless form, it is written as:

$$\frac{F_z}{\frac{1}{2}\rho V_\infty^2 A_{1d}} = \left(1 - \frac{V_{1d}}{V_\infty}\right)^2 \tag{6.5.13}$$

In which the only physical parameter of dependence is V_{1d}/V_∞.

Concerning the flow near the fairing, the following is observed. From the (6.5.12) and the definition of F_z, it follows that:

$$\frac{F_z}{\frac{1}{2}\rho V_\infty^2 A_{1d}} = \frac{-\iint_{A_n}(p - p_\infty)dA_n}{\frac{1}{2}\rho V_\infty^2 A_{1d}} = -\frac{1}{A_{1d}}\iint_{A_n} C_P dA_n \tag{6.5.14}$$

where C_P is the fairing pressure coefficient. Since $F_z > 0$, it must be:

$$\iint_{A_n} C_P dA_n < 0 \tag{6.5.15}$$

From (6.5.15), it can be concluded that this model of fairing behaves as the suction side of an airfoil. Hence, the flow undergoes a convective acceleration along its outer surface.

Considering an elementary streamtube immediately external to the boundary layer of the fairing, then:

$$p_\infty + \frac{\rho V_\infty^2}{2} = p + \frac{\rho V^2}{2} \tag{6.5.16}$$

where fluid properties on the right-hand side are referred to a generic point between A_{hl} and A_m. So:

$$C_P = \frac{p - p_\infty}{\frac{1}{2}\rho V_\infty^2} = \frac{V_\infty^2 - V^2}{V_\infty^2} = 1 - \left(\frac{V}{V_\infty}\right)^2 \tag{6.5.17}$$

An uniform velocity profile along the forebody intake is supposed. This assumption is a major simplification. Yet, it was considered acceptable for a first estimate of p_{2d}. Then, with reference to the external flow $V = V_{max}$ in every point between A_{hl} and A_m. Hence:

$$\frac{F_z}{\frac{1}{2}\rho V_\infty^2 A_{1d}} = -\frac{1}{A_{1d}}\iint_{A_n} 1 - \left(\frac{V_{max}}{V_\infty}\right)^2 dA_n = -\frac{\left[1 - \left(\frac{V_{max}}{V_\infty}\right)^2\right]A_n}{A_{1d}} \tag{6.5.18}$$

Equating the last expression with the one on the right-hand side of (6.5.13) and considering that $A_n = A_m - A_{1d}$:

$$-\Big[1 - \Big(\frac{V_{max}}{V_\infty}\Big)^2\Big]\Big(\frac{A_m}{A_{1d}} - 1\Big) = \Big(1 - \frac{V_{1d}}{V_\infty}\Big)^2 \tag{6.5.19}$$

With reference to figure 6.3, between $A_{\infty,int}$ and A_{1d} continuity can be written: $V_{1d}/V_\infty = A_{\infty,int}/A_{1d}$. Substituting in 6.5.19 and solving with respect to the ratio $A_{\infty,int}/A_{1d}$, it is found that:

$$\frac{A_{\infty,int}}{A_{1d}} = 1 - \sqrt{\Big[\Big(\frac{V_{max}}{V_\infty}\Big)^2 - 1\Big]\Big(\frac{A_m}{A_{1d}} - 1\Big)} \tag{6.5.20}$$

V_{max}/V_∞ is called *supervelocity ratio.* This quantity can be estimated as a function of fairing geometry. In fact, several low speed experimental and theoretical studies relating to streamlined bodies indicate that [36]:

$$\frac{\Delta V}{V} = \frac{V_{max} - V_\infty}{V_\infty} = \frac{1}{2}\Big(\frac{t_{eq}}{l_{eq}}\Big)^{4/3} \tag{6.5.21}$$

where t_{eq} and l_{eq} are *equivalent forebody thickness* and *length*, respectively. Referring to figure 6.4, let us consider an idealized body symmetrical with respect to the A_m plane whose shape is identical to that of the fairing sketched ibidem. Then, t_{eq} is its maximum thickness and l_{eq} its axial extension. Considering numerical values of table 10, it was set: $t_{eq} = D_m - D_{hl}$. Instead, from figure 6.4, it follows that: $l_{eq} = 2l_{max}$. Using these definitions:

$$\frac{\Delta V}{V} = \frac{V_{max} - V_\infty}{V_\infty} = \frac{1}{2}\Big(\frac{D_m - D_{hl}}{2l_{max}}\Big)^{4/3} \tag{6.5.22}$$

From which the ratio V_{max}/V_∞ is found:

$$\frac{V_{max}}{V_\infty} = 1 + \frac{1}{2}\Big(\frac{D_m - D_{hl}}{2l_{max}}\Big)^{4/3} \tag{6.5.23}$$

Substituting (6.5.23) in (6.5.20), an estimate of $A_{\infty,int}$ is found:

$$A_{\infty,int} = A_{1d}\left(1 - \sqrt{\Big\{\Big[1 + \frac{1}{2}\Big(\frac{D_m - D_{hl}}{2l_{max}}\Big)^{4/3}\Big]^2 - 1\Big\}\Big(\frac{A_m}{A_{1d}} - 1\Big)}\right) \tag{6.5.24}$$

6.6 Diffuser Flow Model Results

In previous sections flows inside the diffuser and around the fairing were examined. Results of these analyses are summed up in equations (6.4.1), (6.4.2), (6.4.3) and (6.5.24). These are reproduced below:

$$\begin{cases} \dot{m} = \rho V_\infty A_{\infty,int} \\ p_\infty + \dfrac{\rho V_\infty^2}{2} = p_{1d} + \dfrac{\rho V_{1d}^2}{2} \\ p_{2d}/\rho + V_{2d}^2/2 - (p_\infty/\rho + V_\infty^2/2) + e_{2d} - e_{1d} = 0 \\ A_{\infty,int} = A_{1d}\left(1 - \sqrt{\left\{\left[1 + \frac{1}{2}\left(\dfrac{D_m - D_{hl}}{2l_{max}}\right)^{4/3}\right]^2 - 1\right\}\left(\dfrac{A_m}{A_{1d}} - 1\right)}\right) \end{cases}$$

In which the four unknowns are V_∞, $A_{\infty,int}$, p_{1d} and p_{2d}. Solving the system of equations, it is found:

$$\begin{cases} V_\infty = \dfrac{\dot{m}}{\rho A_{\infty,int}} \\ p_{1d} = p_\infty + \dfrac{1}{2}\rho(V_\infty^2 - V_{1d}^2) \\ p_{2d} = p_\infty + \dfrac{1}{2}\rho(V_\infty^2 - V_{2d}^2) - (e_{2d} - e_{1d}) \\ A_{\infty,int} = A_{1d}\left(1 - \sqrt{\left\{\left[1 + \frac{1}{2}\left(\dfrac{D_m - D_{hl}}{2l_{max}}\right)^{4/3}\right]^2 - 1\right\}\left(\dfrac{A_m}{A_{1d}} - 1\right)}\right) \end{cases}$$

Entering data of table 12, the following results are obtained:

$$\begin{cases} V_\infty = 85\text{m/s} \\ p_{1d} = 3.537 \times 10^6\text{Pa} \\ p_{2d} = 3.580 \times 10^6\text{Pa} \\ A_{\infty,int} = 5.12 \times 10^{-3}\text{m}^2 \end{cases} \tag{6.6.1}$$

A discussion of these values follows.

V_∞ value is consistent with the high-speed application of the waterjet in question. Considering that $V_\infty = V_s$, from figure 3.6 it can be argued that its

Symbol	Value	Unit	Expression
D_{1d}	0.65	dm	-
D_m	2.3	dm	-
D_{hl}	0.83	dm	-
l_{max}	0.5	dm	-
ρ	997	kg/m^3	-
D_e	0.53	dm	-
D_i	15	cm	-
$\overline{V}_{z1}$	18	m/s	-
Q_v	3.4×10^{-1}	m^3/s	$Q_v = \overline{V}_{z1}\frac{\pi}{4}(D_e^2 - D_i^2)$
$\dot{m}$	3.37×10^2	kg/s	$\dot{m} = \rho Q_v$
p_∞	1.01×10^5	Pa	-
V_{1d}	1.05×10^1	m/s	$V_{1d} = Q_v/\frac{\pi}{4}D_{1d}^2$
V_{2d}	0.66×10^1	m/s	$V_{2d} = (1 - \frac{1}{(D_e/D_i)^2})\overline{V}_{z1}$
C_{PR}	0.3	-	-
$e_{2d} - e_{1d}$	29	J/kg	$e_{2d} - e_{1d} = \frac{1}{2}[(1 - C_{PR})V_{1d}^2 - V_{2d}^2]$

Table 12: *Data for solving the system.*

design point is displaced well above vessel speeds typically reachable by these propulsive systems. For these speed values, a very high drag on the entire surface exposed to water is expected. Such a hydrodynamic resistance can jeopardize in-design value of waterjet propulsive efficiency. In fact, as this drag increases, the net waterjet thrust T decreases. From (3.2.1), efficiency drop is explained. An innovative solution was conceived for this issue. It ensures low drag values even at particularly high vessel speeds. However, for confidentiality reasons, details are omitted.

Value obtained for $A_{\infty,int}$ is consistent with the ram-type intake chosen. Indeed, the ratio $A_{1d}/A_{\infty,int} = 4$. Thus, captured streamtube shape is diverging. This means that starting from undisturbed conditions, fluid velocity decreases before entering the diffuser. A static pressure recovery is associated with this convective deceleration. This effect is typical of pods-type intake and is called *ram compression* [7]. Incoming flow velocity regulation takes also place with this process for these diffusers.

$p_{2d} - p_{1d}$ value is consistent with that obtained from the experimental data of figure 6.2. Moreover, ram to diffuser pressure increase is equal to 80. Thus, velocity regulation occurs mainly through external deceleration. This result is consistent once C_{PR}, V_∞ and $\overline{V}_{z1}$ values are considered.

6.7 Numerical Model Adjustment

Using results of section 6.6, numerical model settings of section 5 can be adapted. Indeed, if p_{2d} is known, then static pressure value upstream of the impeller can be estimated.

For this purpose, let us consider the fluid control volume included between the diffuser outflow section, A_{2d} and the impeller inlet: $A_1 = \pi(D_e^2 - D_i^2)/4$. With a proper extension, hypotheses 1-7 of section 6.2 can be accepted. This follows from discussions in sections 6.2, 4.2.1, 5.4 and 5.5. Furthermore, flow between A_{2d} and A_1 can be assumed isentropic. This hypothesis is legitimate if the magnitude of the hydrodynamic losses therein is negligible with respect to those inside the diffuser, i.e. between sections A_{1d} and A_{2d}. This fact was considered licit. In fact, the ratio between control volume axial extension and diffuser length N is less than 10^{-1}. Hence, Bernoulli can be written:

$$p_{2d} + \frac{\rho V_{2d}^2}{2} = p_1 + \frac{\rho V_1^2}{2} \tag{6.7.1}$$

with $V_1 = \overline{V}_{z1}$. Hence p_1 is obtained:

$$p_1 = p_{2d} + \frac{1}{2}\rho(V_{2d}^2 - V_1^2) \tag{6.7.2}$$

In details: $p_1 = 3.56 \times 10^6\text{Pa}$. This parameter heeds internal and external diffusion process. Thus, it can be implemented in the numerical model of section 5. In particular, boundary conditions of section 5.6 have been modified as follows.

Inlet. At the inflow of the control volume defined in section 5.2 the total pressure value measured by a fixed observer was imposed:

$$p_1^0 = p_1 + \frac{1}{2}\rho\overline{V}_{z1}^2 \tag{6.7.3}$$

At the same time, absolute velocity vector was imposed therein: $\overrightarrow{V}_1 = \big(\overline{V}_{r1}, \overline{V}_{\theta 1}, \overline{V}_{z1}\big) = \big(0, 0, 18\big)\text{m/s}$. As for section 5.6, a uniform velocity distribution was assumed. The simplification that results from this choice has already been discussed in section 5.2. From the previous equation, it follows that the two specified conditions fix static pressure value upstream of the impeller. It was decided to impose the total pressure value instead of the static one to enhance numerical stability of the code [24].

Outlet. If the theoretical model of section 4 had been consistent, then known p_1 it would have been possible to estimate static pressure value at the impeller exit. Together with velocity vector or mass flow rate specification at the inlet, these two conditions would have been the most robust set of boundary conditions. Yet, because of this lack of information, mass flow rate was imposed at the outlet. This choice is the only one that consider impeller design conditions. Strictly, average normal speed could have been imposed, too. In fact, this ensures the same robustness [24]. From:

$$Q_{vn} = \frac{1}{N_b}\overline{V}_{z2}\frac{\pi}{4}(D_e^2 - D_i^2) \tag{6.7.4}$$

and because $\overline{V}_{z2} = \overline{V}_{z1}$, it is observed that once impeller geometry is fixed, the imposition of Q_{vn} or $\overline{V}_{z2}$ determines the other. Thus, the two conditions are equal.

Based on section 5 discussions, the remaining aspects of the numerical model were considered valid. Hence, for simplicity, other choices were kept.

6.8 Results Discussion

Table 13 shows the results obtained from the modified numerical model as specified in section 6.7. To ease the comparison, respective values observed in the initial numerical model are also reported. Results of the initial numerical model are denoted with the subscript i. Instead, the ones referring to the adjusted are designated with a. Similarly to section 5.7, if an expression is provided, then the relative value was calculated so. Otherwise, its calculation was done directly through the user interface of the CFD-Post software.

To quantify differences between results, the following expression was used for the relative error of table 13:

$$e_r = \frac{X_{ni} - X_{na}}{X_{na}} \tag{6.8.1}$$

Where X_{ni} is the generic parameter as calculated from model i and X_{na} the one relative to the modified a. The same compatibility criteria specified in section 5.7 are adopted. This fact is motivated by the same reasons discussed therein.

Relevant remarks follows.

Parameter	Unit	Values		Relative error [%]	Expression
		Numerical i	Numerical a		
g	m/s^2	9.81		-	-
ρ	kg/m^3	997		-	-
D_e	dm	0.83		-	-
ω	rad/s	119		-	-
$Q_{v,n}$	m^3/s	4.09×10^{-1}	4.09×10^{-1}	0	-
$\overline{V}_{z1}$	m/s	14	15	0	-
$\overline{V}_{\theta 1}$	mm/s	-7.6	-13	-40	-
$\overline{V}_{r1}$	mm/s	1.1	3.3	-130	-
$\overline{q}_1$	bar	1.81	1.72	-0.5	$\frac{1}{2}\rho(\overline{V_{z1}^2+V_{\theta 1}^2+V_{r1}^2})$
$\overline{p}_1$	bar	0.91	35.6	-100	-
$\overline{p}_1^0$	bar	2.52	37.2	-93	$\overline{p}_1+\overline{q}_1$
$\overline{V}_{z2}$	m/s	15.2	16.2	0	-
$\overline{V}_{\theta 2}$	m/s	-7.2	-7.1	1.3	-
$\overline{V}_{r2}$	mm/s	7.19	8.12	-11	-
$\overline{q}_2$	bar	2.95	2.95	0.2	$\frac{1}{2}\rho(\overline{V_{z2}^2+V_{\theta 2}^2+V_{r2}^2})$
$\overline{p}_2$	bar	2.27	36.9	-94	-
$\overline{p}_2^0$	bar	4.22	38.8	-90	$\overline{p}_2+\overline{q}_2$
h	m	17	16.8	3.4	$\dfrac{\overline{p}_2^0-\overline{p}_1^0}{\rho g}$
$\overline{r_1 V_{\theta 1}}$	m^2/s	-6.3×10^{-4}	-1.4×10^{-3}	-55	-
$\overline{r_2 V_{\theta 2}}$	m^2/s	-4.87×10^{-1}	-4.84×10^{-1}	0.5	-
h_t	m	21	21	0.4	$\dfrac{\omega(\lvert\overline{r_2 V_{\theta 2}}\rvert-\overline{r_1 V_{\theta 1}})}{g}$
η_{id}	-	0.5	0.71	3	h/h_t
ϕ	-	0.869	0.870	0.1	$\overline{V}_{z1}/(\omega\frac{D_e}{2})$
ψ	-	0.22	0.21	3	$gh/(\omega\frac{D_e}{2})^2$
ψ_t	-	0.34	0.34	0.4	$gh_t/(\omega\frac{D_e}{2})^2$
N_s	-	7	5	-2.5	$\omega\sqrt{Q_{v,n}}/(gh)^{0.75}$

Table 13: *Comparison between results of the two numerical models.*

*Label i refers to the **initial** model, viz. the one examined in section 5. Instead, a designates the **adjusted** model. Details on latter's setting are specified in section 6.7 . Relative error is defined as in* (6.8.1).

1. Values of $\overline{V}_{\theta 1}, \overline{V}_{r1}, \overline{V}_{r2}$ and $\overline{r_1 V_{\theta 1}}$ are incompatible. Yet, if compared with those relating to the theoretical model in table 9, all values can be considered equal to zero. Thus, compatibility with the theoretical model is achieved in both cases. It is believed that differences observed are due to the different boundary conditions set. Therefore, discrepancies explanation relies in numerical facts rather than physical;

2. Except for $\overline{p}_1, \overline{p}_2, \overline{p}_1^0$ and $\overline{p}_2^0$, all the remaining values of model a are compatible with those relating to model i.

   This fact can be justified as follows. In section 3.2.2 it was seen that impeller operation can be summed up by the following relationships:

   $$\begin{cases} \eta_{id} = f(\phi) \\ \psi = f(\phi) \end{cases}$$

   where ϕ is given by (3.2.3). With reference to this last expression, it should be noted that $\overline{V}_{z1}$ in the model i was imposed. Besides, the value obtained from model a is compatible with model i. This can be clarified using continuity equation. Indeed, from (5.6.1):

   $$\overline{V}_{z1} = \dot{m}_n N_b / \left[\rho \frac{\pi}{4} (D_e^2 - D_i^2) \right] \tag{6.8.2}$$

   Mass and so volumetric flow rate value was set identical for the two models. In addition, blade geometry and angular velocity is identical. Then, from the (6.8.2) follows the compatibility on $\overline{V}_{z1}$. These facts explains ϕ equality. Hence, the same η_{id} and ψ values are also expected. Thus, the simulated operation of the two impellers is the same.

   In Figure 5.4 it can be seen that model i predicts a cavitating region. Accordingly, a fluid region of different aggregation state is expected. Yet, from the above compatibilities, it follows that this volume did not induce changes in the resulting flow. Reason lies in hypothesis 2 of section 5.5. Due to this assumption, the cavitating region is treated similarly as the liquid phase. Thus, the absence of deviations in mean flow parameters is due to numerical model incapacity to contemplate cavitation effects;

3. $\overline{p}_1$ and $\overline{p}_1^0$ for model a are compatible with those of the theoretical model developed in this section. This represents a further data verification;
4. Based solely on data possessed, it is impossible to establish whether $\overline{p}_2$ and $\overline{p}_2^0$ for model a are plausible. In fact, because of theoretical model inconsistencies, reference data lack.

From the last point discussed, it is evident the necessity of reference data. These would be valuable for results comparison. Those relating to kinematics in outflow section are particularly interesting. If available data are beheld, then it is possible to compare theoretical and numerical β_{2k} values. In fact, considering the adjustment $i_k \propto (D_e - D_i)$, theoretical values can be estimated through (4.4.1):

$$\beta_{2k} = \gamma_k + |\theta_{2k}| - \delta_k \tag{6.8.3}$$

where γ_k can be expressed as:

$$\gamma_k = \beta_{1k} + i_k + \theta_{1k} \tag{6.8.4}$$

hence:

$$\beta_{2k} = \beta_{1k} + i_k + \theta_{1k} + |\theta_{2k}| - \delta_k = \beta_{1k} + i_k + \theta_{ck} - \delta_k \tag{6.8.5}$$

In which $\beta_{1k} = \arctan(\overline{V}_{z1}/U_{1k})$. Near hub and shroud, viscous phenomena are expected to be relevant. For this reason, the comparison was referred exclusively to the three internal blade sections. Inserting in (6.8.5) values of table 3 and 4, β_{2k} theoretical values are found. These are compared with those provided by numerical models in the following table.

Normalized span	β_{2k} [°]			Relative error [%]	
	Theoretical	Numerical a	Numerical i	Numerical a	Numerical i
0.25	54.77	54.83	54.48	-0.1	0.5
0.5	46.35	46.41	44.11	-0.1	5.1
0.75	42.40	42.46	38.62	-0.1	9.8

Table 14: *Comparison between theoretical and numerical values of relative fluid angle at the impeller outlet.*

Label i refers to the ***initial*** *model, viz. the one examined in section 5. Instead, a designates the* ***adjusted*** *model. In both cases, relative error is defined as in* (5.7.1).

All values related to model a are compatible with those of the theoretical model. This supports the plausibility of model a results. It can be also noted that model i values are incompatible as far as higher radii blade sections are concerned. Reminding figure 5.4, this fact lead to the following conclusion. Cavitating region extension affects average fluid properties relative to the single cylindrical sections. Hence, cavitation effects are contemplated in the numerical model, albeit in reduced terms.

In conclusion, relevant results can be summed up in following points.

A. Compatibility between energy-exchange related values of the two numerical models attest that even in the modified numerical model these values are incompatible with those of the theoretical model. Once again, this results from the *a posteriori* adjustment on incidence made in the preliminary design;

B. In the modified numerical model, the cavitation phenomenon is absent. In fact, minimum absolute static pressure value is found to be: $p_{min} = 2.41 \times 10^6\text{Pa}$. This is necessary for the model to represent the real impeller operation;

C. Available theoretical data support modified numerical model results. Thus, the simulated flow can be considered plausible. Yet, these data prevent to conclude that this flow can be observed for the specified operating conditions. This is due to the poorness of comparison data available in the theoretical model. This issue could be solved by collecting experimental data related to the in-design operation of the impeller. In particular, a test-facility could be developed. Average inlet static pressure and mass flow rate could be set equal to those of theoretical model. Once angular velocity has been set, average static pressure value observed at the outlet could be measured. Compatibility with those data would confer the reliability of numerical model results.

7 Conclusions

Following facts emerged from an overview of the waterjet propulsion system.

1. Waterjet propulsion reaches vessel speed values that are precluded for marine propeller. This is shown in Figure 3.6. Besides, the figure shows that high vessel speed can be obtained with a propulsive efficiency even higher than the greatest of all propeller systems. This increase has a decisive impact on power-train consumption and thus on its emissions. Today, this aspect is fundamental;
2. Waterjet propulsion asks for a greater space for its installation than the marine propeller system does. Hence, it is also heavier. Furthermore, the greater number of components implies a lower reliability of the plant. In addition, greater costs for design, engineering and manufacturing are expected.

The extent of the defects related to point 2 can be contained by arranging the entire propulsion system around a single axis. Following this solution, a ram type inlet is necessarily adopted. Present work was made precisely with reference to this waterjet framework. Further, its design was developed specifically for very high vessel speed.

With reference to the aforementioned waterjet, this work has addressed mechanical and hydrodynamic issues related to its design. Mechanical problems treatment would necessarily imply confidential data diffusion. For this reason, this part has been omitted entirely.

Sections 4 and 5 examined theoretical preliminary design model of the impeller and numerical model relative to the prediction of its in-design behavior. The purpose was to understand reasons behind the incompatibility between the two models found by the designer.

Section 4 analysis was addressed as follows. First, a reference theoretical model was analyzed in detail. All its assumptions were critically discussed before being accepted. Subsequently, the method actually followed by the designer was examined. Differences found between the two procedures were highlighted. Results survey of the method followed by the designer remarked an inconsistency in its assumptions. In particular, it was found that the relationship (4.4.1) between blade profile angles is not respected. Residual scrutiny reported in Table 4 led to following conclusion. The reason behind this inconsistency was related to the *a posteriori* adjustment made on incidence. Finally, it was shown that this change contrasts with the fundamental assumption underlying the entire design procedure. This consists in the choice of a desired swirl profile downstream of the impeller. This fact prevented the unique resolution of inconsistencies found.

Section 5 analyzed in depth main points of the numerical model development. These include control volume definition, mesh generation and numerical code setting. All the assumptions were widely discussed before being considered reasonable. Numerical values of the fundamental data used for the model development were reported. Finally, compatibility between theoretical and numerical model results was surveyed. This was done in simplified terms. In fact, uncertainty analysis was completely neglected. Still, the subjective criterion adopted on the maximum relative error tolerable allowed highlighting following facts.

A. The set of boundary conditions imposed was considered coherent.

This fact derives from the compatibility with the theoretical model of the values assumed by the components of the absolute velocity vector $\overrightarrow{V}_1 = \left(\overline{V}_{r1}, \overline{V}_{\theta 1}, \overline{V}_{z1}\right)$ and of the volumetric flow rate Q_{vn}. All numerical values are shown in table 9. Consequently, the parameters that summarize impeller operation relative to kinematics are compatible. In table 9, this can be deduced from the observation of the values assumed by the flow coefficient ϕ;

B. All quantities associated with impeller energy exchange were deemed incompatible.

This can be deduced from the observation of the value assumed by the pressure coefficient ψ in table 9. Reason for this was due to the later change made in incidence at the preliminary design stage;

C. Based on the data possessed, it was not possible to justify hydraulic efficiency η_{id} compatibility observed in table 9. In fact, the assignment criterion used in the preliminary design was concealed;

D. Inlet and outlet fluid thermodynamic state predicted by the numerical model is unreal.

$\overline{p}_1$ value form table 9 justifies this statement. In fact, this is lower than atmospheric pressure value. This contrasts with the in-design diffusive action operated by the intake. Due to pressure recovery that takes place upstream and inside the diffuser, fluid average static pressure downstream of it is expected to be higher than atmospheric;

E. The fact discussed in previous point led to the identification of a cavitation region sketched in figure 5.4.

Yet, from section 5.7 discussion, it was shown that this phenomenon is unexpected at the design point. Underlying reason was assigned to an improper choice of boundary conditions. Indeed, it was shown that from continuity point of view these are sufficient but not necessary.

Yet, from force-balance point of view, they are insufficient to represent expected physical phenomenon.

To solve issue of point **E**, in section 6 a theoretical model was developed. The aim was to estimate average static pressure value upstream of the impeller. The only data used were those available in previous sections. This model analyzed flow inside the diffuser and outside the waterjet fairing. Experimental results of aeronautics were used. Yet, legitimacy of their use was first discussed. All the simplifying hypotheses adopted were widely discussed. Results of the theoretical model thus obtained were commented. Once their validity was accepted, they were used to adjust the numerical model analyzed in section 5. Finally, results obtained were compared with those relating to the initial numerical model. Same compatibility criteria relating to section 5 were used.

Main conclusions are summarized below.

A. Compatibility between impeller energy-exchange quantities of the two numerical models were attributed. This can be argued from ψ values observation in table 13. This fact confirmed the incompatibility of the modified numerical model with the initial theoretical one. Reason was due to the *a posteriori* modification on incidence;

B. In the modified numerical model, cavitation phenomenon is absent. With reference to the initial numerical one, this is an improvement;

C. Values of $\overline{p}_1$ and $\overline{p}_1^0$ relating to the modified numerical model are compatible with those of the theoretical model developed in section 6. In addition compatibility in outflow fluid relative angles β_{2k} at inner blade sections was achieved. This can be argued from table 14 analysis.

Thus, simulated flow can be considered plausible. Yet, deficiency in reference data prevented the conclusion that this could be also reliable.

References

[1] J. Carlton, *Marine propellers and propulsion.* Butterworth-Heinemann, 2018.

[2] C. Kruppa, “Wasserstrahlantriebe f¸r hochgeschwindigkeits-fahrzeuge,” *Technischen Universit‰ t Berlin, 16e Jahrgang Jahrbuch Schiffbau Technisches Gesellschaft, Band 62*, 1972.

[3] Y. A. Cengel, *Fluid mechanics.* Tata McGraw-Hill Education, 2010.

[4] L. Yun and A. Bliault, *Theory and design of air cushion craft.* Elsevier, 2000.

[5] W. Commons, “File:electricity production in the world.png — wikimedia commons, the free media repository,” 2016, [Online; accessed 24-September-2019]. [Online]. Available: https://commons.wikimedia.org/w/index.php?title=File:Electricity_production_in_the_World.PNG&oldid=196438901

[6] S. L. Dixon and C. Hall, *Fluid mechanics and thermodynamics of turbomachinery.* Butterworth-Heinemann, 2013.

[7] S. Farokhi, *Aircraft propulsion.* John Wiley & Sons, 2014.

[8] Wikipedia contributors, “World energy consumption — Wikipedia, the free encyclopedia,” 2019, [Online; accessed 24-September-2019]. [Online]. Available: https://en.wikipedia.org/w/index.php?title=World_energy_consumption&oldid=916479049

[9] D. Küchemann and J. Weber, *Aerodynamics of propulsion.* McGraw-Hill, 1953.

[10] J. Seddon and E. L. Goldsmith, *Intake aerodynamics.* AIAA education series, 1999.

[11] N. W. H. Bulten, "Numerical analysis of a waterjet propulsion system," 2006.

[12] D. Papale, "High performance waterjets: study of an innovative scoop inlet and development of a novel method to design ducted propellers." 2015.

[13] R. Svensson, "Experience with the kamewa water jet propulsion system," in *Advanced Marine Vehicles Conference*, 1989, p. 1440.

[14] J. Allison, "Marine waterjet propulsion," 1993.

[15] N. Warren, J. Kecsmar, and N. Sims, "Waterjet propulsion-a shipbuilder's view," 1994.

[16] J. B. Heywood, "Internal combustion engine fundamentals," 1988.

[17] Energy Information Administration (EIA), 2019. [Online]. Available: https://www.eia.gov/

[18] G. Ventrone, *Macchine per allievi ingegneri.* Libreria internazionale Cortina, 2006.

[19] A. J. Stepanoff, "Centrifugal and axial flow pumps," *Theory, Design, and Application*, 1957.

[20] A. Howell, "Fluid dynamics of axial compressors," *Proceedings of the Institution of Mechanical Engineers*, vol. 153, no. 1, pp. 441–452, 1945.

[21] E. Dick, *Fundamentals of turbomachines.* Springer, 2015, vol. 109.

[22] C. Berbente, I. C. Andrei, N. M. Ene, F. Frunzulica, and E. Korody, “Special topics on map meshing in turbomachinery,” *Periodica Polytechnica Transportation Engineering*, vol. 34, no. 1-2, pp. 59–68, 2006.

[23] H. K. Versteeg and W. Malalasekera, *An introduction to computational fluid dynamics: the finite volume method.* Pearson education, 2007.

[24] A. Fluent, “19.2 theory guide.(2018), ansys.”

[25] F. R. Menter, “Performance of popular turbulence model for attached and separated adverse pressure gradient flows,” *AIAA journal*, vol. 30, no. 8, pp. 2066–2072, 1992.

[26] F. R. Menter, M. Kuntz, and R. Langtry, “Ten years of industrial experience with the sst turbulence model,” *Turbulence, heat and mass transfer*, vol. 4, no. 1, pp. 625–632, 2003.

[27] D. C. Wilcox *et al.*, *Turbulence modeling for CFD.* DCW industries La Canada, CA, 1998, vol. 1,2.

[28] J. E. Bardina, P. G. Huang, and T. J. Coakley, “Turbulence modeling validation, testing, and development,” 1997.

[29] J. D. Anderson Jr, *Fundamentals of aerodynamics.* Tata McGraw-Hill Education, 2010.

[30] G. Cornetti, *Macchine a fluido.* Il capitello, 1993.

[31] N. Krasnov, “Aerodynamics,” Tech. Rep.

[32] B. Munson, D. Young, and T. Okiishi, “Fundamentals of fluid mechanics,” 1998.

[33] B. S. Massey and J. Ward-Smith, *Mechanics of fluids.* Crc Press, 1998, vol. 1.

[34] M. Bhatti, "Rk shah,"turbulent and transition flow convective heat transfer, handbook of single-phase convective heat transfer," 1987.

[35] S. J. Kline, D. E. Abbott, and R. W. Fox, "Optimum design of straight-walled diffusers," *Journal of Basic Engineering*, vol. 81, no. 3, pp. 321–329, 1959.

[36] S. F. Hoerner, "Fluid-dynamic drag," *Hoerner fluid dynamics*, 1965.